# Interfacial engineering of metal chalcogenide-based heterostructures for advanced sodium-ion batteries

*Yuxiang Zhang, Bo Han, Shuangshuang Tan, Qiang Gao, Zhao Cai, Chenggang Zhou, Jiantao Li*, Ruimin Sun*, Khalil Amine**

Y. Zhang, B. Han, Q. Gao, Z. Cai, C. Zhou, R. Sun
Faculty of Materials Science and Chemistry, China University of Geosciences (Wuhan), Wuhan 430074, China. E-mail: rmsun@cug.edu.cn

S. Tan
College of Materials Science and Engineering, Chongqing University, Chongqing, 400045, China.

J. Li, K. Amine
Chemical Sciences and Engineering Division, Argonne National Laboratory, Lemont, IL 60439, USA. E-mail: jiantao.li@anl.gov, amine@anl.gov

K. Amine
Pritzker School of Molecular Engineering, The University of Chicago, Chicago, IL 60637, USA.

**Keywords:** metal chalcogenide, heterostructures, anode, sodium-ion batteries

**Abstract:** Sodium-ion batteries (SIBs) have become one of the most promising candidates for large-scale energy storage applications. Metal chalcogenides anode materials based on alloying or conversion reactions have been widely studied because of their high theoretical capacities and rich redox reactions. However, their intrinsic limitations such as high voltage hysteresis and large volume expansion hinder their further applications. The construction of heterostructures has become an attractive strategy to alleviate the above issues. The formation of built in electric fields (BIEFs) at the heterointerfaces will accelerate the migration of $Na^+$ and electrons. Moreover, heterostructures can also enhance the structural stability, generate more active sites and provide additional capacity. It is worth noting that heterointerfacial properties play a significant role in promoting the overall electrochemical performance of the heterostructures. However, a systematic understanding of their interfacial engineering is currently lacking. This article reviews the research progress of metal chalcogenide based heterostructure anode materials in the near term. Firstly, the definition, classification and the roles of heterostructures are introduced. Secondly, the detailed research progress of the metal chalcogenide based heterostructures anodes in SIBs is discussed. Finally, the future prospects and potential research directions of the heterostructures for batteries are discussed.

## 1. Introduction

Lithium-ion batteries (LIBs), as secondary batteries, have dominated the portable electronics market since their commercialization in 1991 and are extensively used in electric vehicles.[1-6] However, owing to the scarcity of lithium resources, alternative energy storage devices need to be developed. SIBs have become one of the most attractive candidates for large-scale energy storage applications due to their abundant sodium resources, low cost, high safety and similar working principles to LIBs. However, compared with LIBs, the large ionic radius of $Na^+$ (1.02 Å for $Na^+$ and 0.67 Å for $Li^+$) causes slow reaction kinetics in electrode materials, thus exhibiting inferior rate performance. In addition, repeated intercalation/deintercalation of $Na^+$ leads to large volume expansion and pulverization of the electrode materials, thus delivering poor cycling stability.[7-10] Therefore, it remains a challenge to find appropriate host materials with high reversible capacity and sufficient structural stability to withstand repeated sodiation/desodiation processes.

For SIBs, great progresses have been made in the research of cathode materials, such as polyanionic compounds, layered oxides, Prussian blue analogs (PBAs).[11-14] However, the development of anode materials has been sluggish. The anode materials can be divided into three categories based on the different reaction mechanisms during redox processes: intercalation-type, conversion-type and alloy-type. [15] Intercalation-type materials such as carbon materials (hard carbon, graphene) and titanium-based materials ($TiO_2$, $Na_2Ti_3O_7$) exhibit small volume expansion and excellent cycling but low specific capacities.[16] Conversion-type (metal oxides, sulfides, selenides, etc.) and alloy-type (Ge, Si, Sn, and Sb) anodes are often accompanied by the multiple electrons reactions during the redox processes, providing higher specific capacities and energy densities. However, they usually undergo huge volume expansions, resulting in severe pulverization and even detachment from the current collectors, leading to rapid capacity fading.[17-19] A large number of research strategies have been proposed to address the above-mentioned issues, such as morphology optimization, compositing with carbon materials, defect engineering and construction of heterostructures. Among them, the construction of heterostructures has attracted extensive attention in the past few years.[20-23]

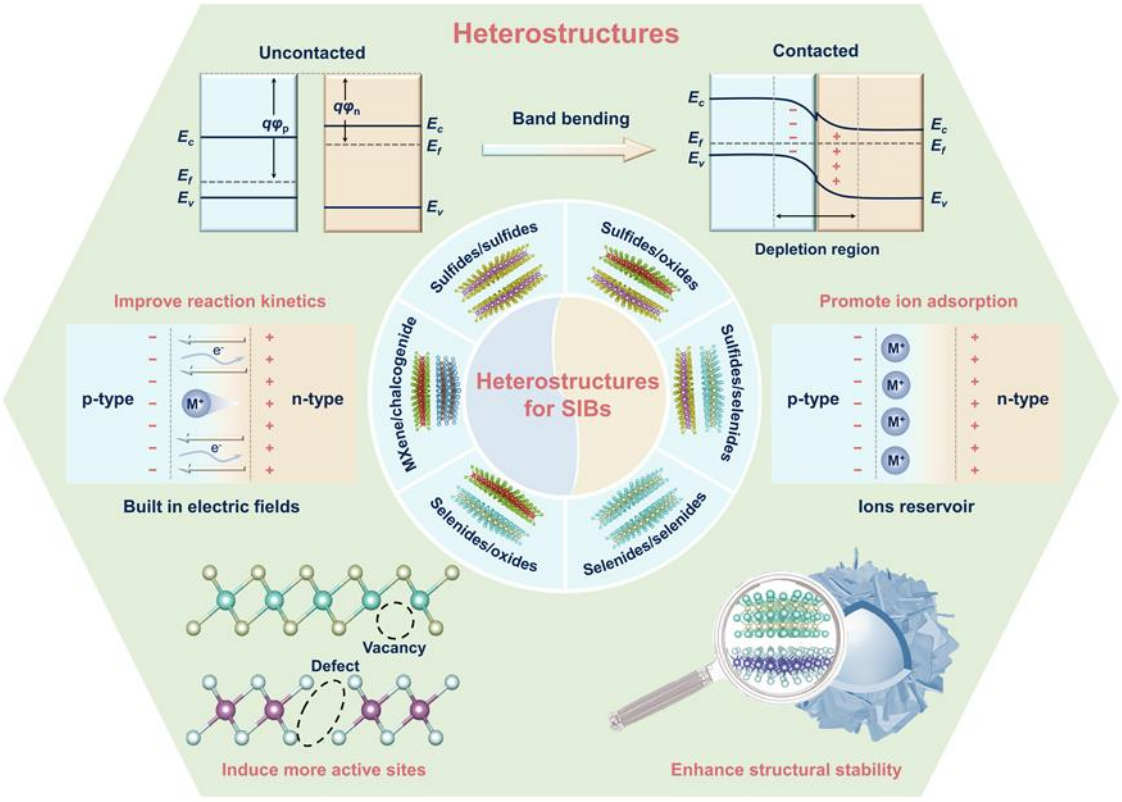


**Figure 1**. Overview of the transition metal chalcogenides-based heterostructures for SIBs.

Heterostructures usually refer to the interface regions formed by two or more materials bonded together through physical (mainly van der Waals force) or chemical interactions. The design of the heterostructures is not simply to combine two materials, but to focuses on the influence of the inherent properties of the building blocks (like semiconductor types, energy band structures, carrier concentrations) on the electronic structures and electric field distributions of the entire materials.[24] When two types of semiconductors come into contact, because of the difference in the band gaps and work functions, carriers will diffuse between the two semiconductors until the Fermi level reaches equilibrium. This process results in the formation of the BIEFs between the two-phase interfaces and causes charge redistribution. Along with the formation of the BIEFs, the electron accumulation regions will present negative potentials, which are conducive to the adsorption of ions and will also accelerate the charge transfer of ions and electrons, thus improving the electrochemical kinetics of the heterostructure materials. In addition, heterostructures can also improve the structural stability of the whole materials, generate more active sites and improve electrochemical reactivity.[25-28]

In recent years, heterostructures are developed rapidly and many new exciting discoveries have been reported. The research progress of heterostructure-type anode

materials has also been reviewed by the related researchers. For example, Gabriel et al.[29] reviewed the current research status of heterostructure type anode and cathode materials for SIBs, focusing on the synthesis methods of the heterostructures. Park et al.[30] reviewed the recent research progress of the heterostructure materials in rechargeable alkali ion ($Li^+$, $Na^+$ and $K^+$) batteries, focusing on the experimental methods to verify the effect of the heterostructure. Du et al.[31] focused on the latest preparation strategies and characterization techniques for heterostructure materials. It is worth noting that heterointerfacial properties play a significant role in promoting the overall electrochemical performance of the heterostructures. Despite the effectiveness of the heterostructure design, a systematic understanding of their interfacial engineering is currently lacking. And the definition and role of heterostructures have not been clearly explained. The related comprehensive reviews, holistic understanding and general popularization of the metal chalcogenide based heterostructures is very necessary. Therefore, this review presents a detailed summary of the latest research status of the metal chalcogenides-based heterostructures in recent years. In this review, firstly, the definition of the heterostructures and the roles of the heterostructures in SIBs are introduced. Secondly, the latest research progress of metal chalcogenides-based heterostructures for SIBs is reviewed. Finally, some brief conclusions and perspectives on the development of transition metal chalcogenides-based heterostructures are provided for the future research. An overview of Interfacial engineering of the metal chalcogenide-based heterostructures for SIBs is shown in **Figure 1**.

## 2. The definition of heterostructures

In recent years, the concept of heterojunction has been widely used in many research fields, including solar cells, semiconductor devices, photoelectrocatalysis and electrochemical energy storage, and so on [32-38]. Heterojunction is usually defined as the interface region formed by the contact of two semiconductors materials with different bandgap widths. When two different semiconductors come into contact, because of the difference in bandgaps and work functions, carriers will diffuse between the two semiconductors until the Fermi level reaches equilibrium. This process will lead to the formation of a depletion region near the two-phase interfaces, inducing the BIEFs at the heterointerfaces, which endow the heterostructure materials with high conductivity under forward bias and almost insulate under reverse bias. In addition, the energy bands bend near the heterointerfaces when the two phases are contacted. The degree of the

energy band bending and the width of depletion region depend on the carrier concentration. Low carrier concentration leads to more severe band bending and wider depletion region. Semiconductor materials can generally be classified into pure semiconductors, n-type and p-type semiconductors. Among them, p-type semiconductors contain higher concentrations of the holes (equivalent to the positive charges) and conduct electricity mainly through holes, while n-type semiconductors usually have higher concentrations of free electrons, mainly conducting electricity through free electrons.[31] According to the different types of semiconductors, heterojunction can be classified as Schottky junction, p-n junction, and p-p or n-n junction.

**2.1 Schottky junction**

Schottky junction refers to the interface between metals and different types of semiconductors and their carriers are only electrons. The work functions of the semiconductors are generally smaller than that of the metals, so when the metals and the semiconductors (n-type, for example) come into contact, electrons will flow from the semiconductors to the metals, forming the depletion regions composed of positively charged immovable impurity ions in the surface layers of the semiconductors, thereby forming the BIEFs directed from the semiconductors to the metals, which prevent the continuous migration of electrons from the semiconductors to the metals (**Figure 2**a). At the interfaces, the energy bands of the semiconductors bend to form the high potential energy regions, namely the Schottky barriers. The electrons must have higher energy to cross these barriers and flow into the metals. When different metals are in contact with different types of semiconductors, they have different Schottky barrier heights. Yang et al. [39] prepared a one-dimensional hollow nanotube material embedded with Cu quantum dots and $Mo_2C/MoO_2$. The formation of the Mott-Schottky heterojunction improved the charge transfer kinetics of the material, thereby improving the sodium storage performance of the material. Yin et al. [40] combined the advantages of metals, metal sulfides and carbon to prepare hollow core-shell Sb/ZnS@C heterostructure materials. The BIEFs formed at the heterointerfaces of Sb and ZnS enhance the $Na^+$ diffusion kinetics. This heterostructure material exhibits excellent sodium storage performance.

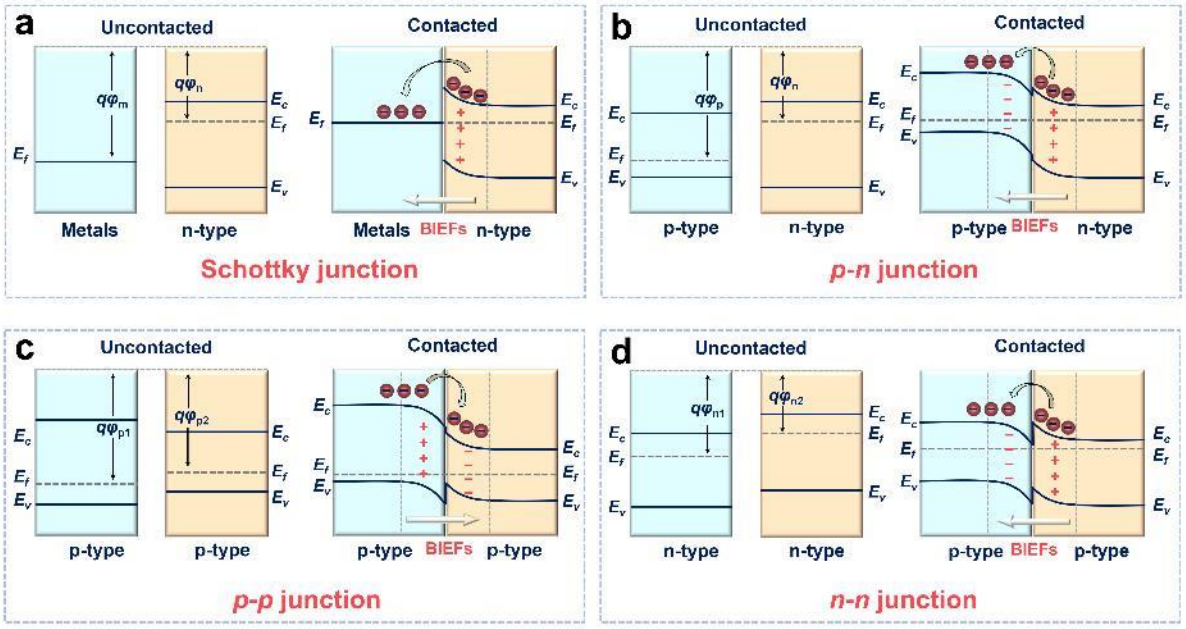


**Figure 2**. Schematic diagram of heterojunction. a) Schottky junction. b) p-n junction. c) p-p junction. d) n-n junction.

### 2.2 p-n junction

Specifically, the p-n junction can be obtained by combining two opposite types of semiconductors (Figure 2b). Different from Schottky junction, the carriers of p-n junction can be either electrons or holes. Once p-type and n-type semiconductors come into contact, the band alignment will initiate spontaneously at the heterointerfaces and the charges near the interfaces will be redistributed. Specifically, electrons in the n-type region will migrate to the p-type region, generating positively charged impurity ions. At the same time, holes in the p-type region will migrate to the n-type region, producing negatively charged impurity ions. Electron-hole migration will continue until the Fermi levels of the systems reach equilibrium, eventually separated by fully ionized depletion regions. This process will induce BIEFs at the interfaces directed from the n-regions to the p-regions. Huang et al.[41] prepared $SnS_2/CoS_2$ heterostructure materials, which showed outstanding rate performance and cyclic stability owing to the formation of p-n junction at the heterointerfaces. Zheng et al. [42] prepared $SnS/SnO_2$ heterostructure by coupling SnS (p-type) and $SnO_2$ (n-type). By utilizing the interface effect of the heterostructure, the ion/electron transfer ability was enhanced, thereby improving the sodium storage performance of the material.

### 2.3 p-p or n-n junction

Homogeneous-type heterojunction is composed of the semiconductors with the same types, usually p-p type (Figure 2c) or n-n type (Figure 2d). Like the p-n junction, there are also depletion regions at the n-n type or p-p type heterointerfaces, but the electron-hole recombination at the interfaces is much lower than that the p-n junction. At present, there are few reports on these homogeneous-type heterojunction in the battery fields.

## 3. The roles of heterostructures in SIBs

Compared with traditional composite materials, heterostructure materials attract much attention due to the positive influence of the heterointerfaces on material properties. Generally, the properties of the heterostructure materials are closely related to the unique microstructures of the heterointerfaces. As mentioned above, when two materials come into contact, because of the difference in their carrier concentrations, electrons will flow unidirectionally at the interfaces, thereby forming the BIEFs. The electron accumulation regions will present negative potentials, which are conducive to the adsorption of ions. In addition, the existence of BIEFs will also accelerate ion migration, thus enhancing the redox reaction kinetics of the heterostructure materials. Generally, heterostructure electrode materials have the advantages of accelerating ion diffusion kinetics, enhancing electrical conductivity, increasing ion adsorption ability, enhancing structural stability and inducing more active sites in battery systems.

### 3.1 Accelerate ion diffusion kinetics

The BIEFs and carrier concentration gradients formed at the heterointerfaces will accelerate the ion diffusion ability, thereby improving the energy storage performance. The migration directions of ions will change along with the discharged/charged states. Assuming that the ion migration direction during the discharged process is consistent with the direction of the BIEFs, this will accelerate the ion migration. During the charged process, the ion migration direction will change and be opposite to the direction of the pristine BIEFs. At this time, the electric fields will hinder the ion migration. In order to resolve this contradiction, some researchers have studied the working mechanisms of the BIEFs. The results demonstrate that the direction of the BIEFs will change reversibly with the intercalation/extraction of the metal ions, so that the material delivers excellent ion diffusion ability in all the redox processes. [42-44]

Zhang et al. [43] prepared $Fe_9S_{10}$@$MoS_2$@C heterostructure materials and the large energy bandgap difference between the two materials can generate a stronger electric

field at the heterointerfaces (**Figure 3**a). When the two phases were in contact, electrons are transferred from $MoS_2$ to the $Fe_9S_{10}$ side, generating a BIEFs directed from $MoS_2$ to $Fe_9S_{10}$. At the same time, the reversibility of the reaction of $MoS_2$ and $Fe_9S_{10}$ with $Na^+$ was compared by calculating the Gibbs free energy change of the sodiation reactions. The results showed that the reversibility of $Fe_9S_{10}$ ($\Delta G = -1.49$ eV) is better than that of $MoS_2$ ($\Delta G = -2.37$ eV). Therefore, during the desodiation process, more $Na^+$ can be transferred from the $Fe_9S_{10}$ side quickly, resulting in the formation of a Na-poor and a Na-rich region at the $Fe_9S_{10}$ and $MoS_2$ sides, respectively. The $Na^+$ concentration difference will produce a reverse electric field from the $Fe_9S_{10}$ to the $MoS_2$, thus promoting the $Na^+$ diffusion ability during the charging process.

Ni et al. [44] prepared $Fe_2O_3/FeS_2$ heterostructure materials, where $Fe_2O_3$ and $FeS_2$ were n-type and p-type semiconductors, respectively. A BIEFs pointing from $Fe_2O_3$ to $FeS_2$ will spontaneously form in the interface regions between the two materials (Figure 3b). During the discharging process, the BIEFs promoted the migration of $Na^+$ from the positively charged side of $Fe_2O_3$ to the oppositely charged side of $FeS_2$, accelerating the ion diffusion kinetics. During the charging process, $Na^+$ was preferentially released from the $Na_2S$ due to the higher reactivity of the discharged product of $Na_2S$ than $Na_2O$, causing the change of the electric field direction. Therefore, the generation of the BIEFs facilitated the $Na^+$ diffusion kinetics during the whole redox process.

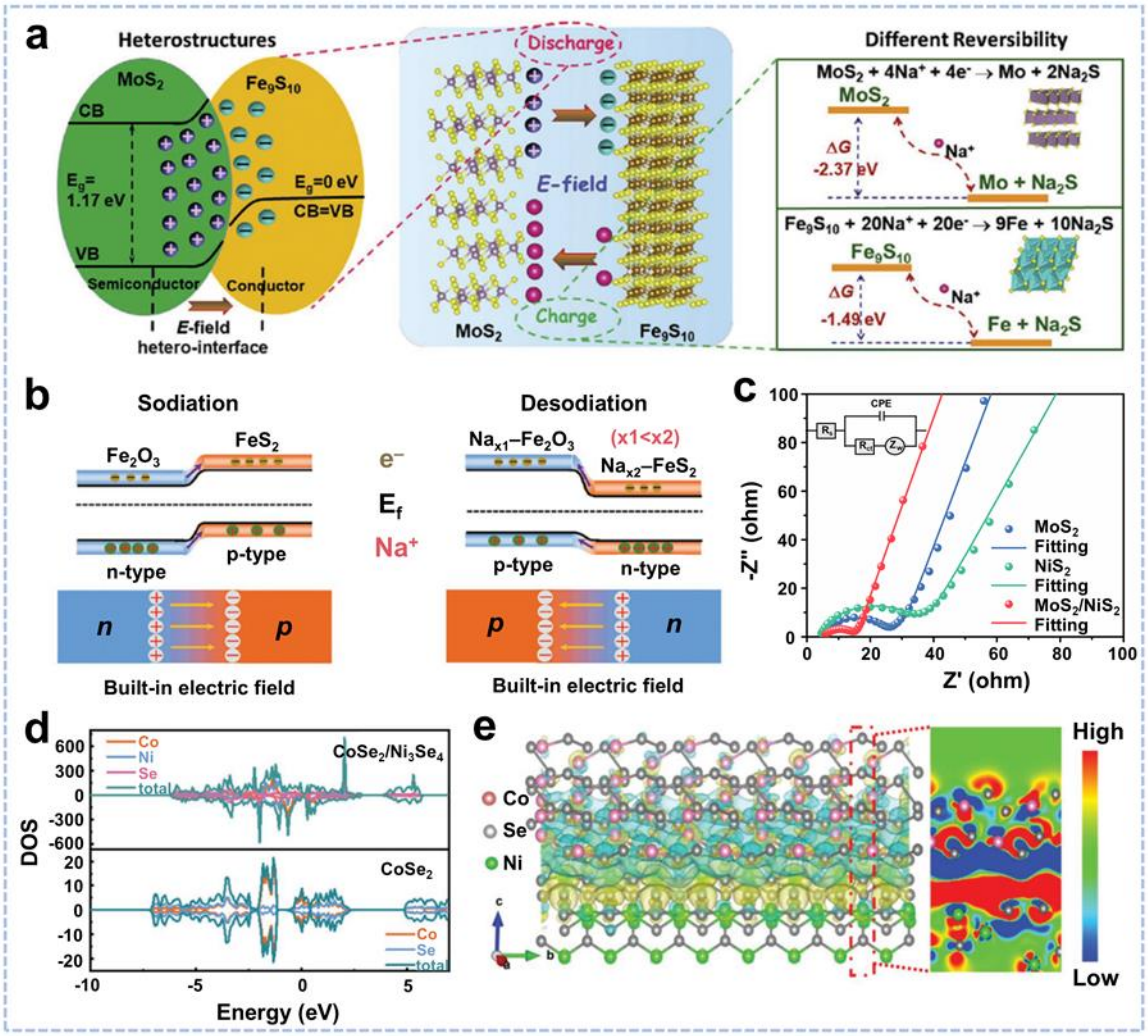


**Figure 3**. a) Schematic diagram of the formation and direction of BIEFs for $Fe_9S_{10}$@$MoS_2$@C heterostructures. Reproduced with permission.[43] Copyright 2020, Elsevier. b) Schematic illustration of the formation of BIEFs and $Na^+$ storage mechanism. Reproduced with permission.[44] Copyright 2019, Wiley-VCH. c) Nyquist curves of $VS_2$/$MoS_2$, $VS_2$, $MoS_2$, and $VS_2$-$MoS_2$ mixture electrodes, respectively. Reproduced with permission.[26] Copyright 2024, Elsevier. d) DOS of $Ni_3Se_4$/$CoSe_2$ and pure $CoSe_2$. e) Charge density difference of the $Ni_3Se_4$/$CoSe_2$ heterostructures. Reproduced with permission.[45] Copyright 2022, Wiley-VCH.

### 3.2 Enhance electric conductivity

The change of energy bands at the interfaces between the two different components can form heterostructures, which can induce the BIEFs with a specific direction, and this process is followed by the rapid transfer of electrons. However, the migration of electrons can also be related to the quantum tunneling effects. In particular, some electrons whose energies are lower than the energy barriers can also reach the interfaces through the

quantum tunneling, thereby recombining with the holes at the heterointerfaces until the Fermi levels reach equilibrium.

Electrochemical impedance spectroscopy (EIS) analysis is often applied to provide the evidence for the enhanced conductivity of the heterostructure materials. Zhang et al. [26] prepared the $MoS_2/NiS_2$ heterostructures and verified the effect of the heterostructures on the $Na^+$ storage kinetics by EIS. As shown in Figure 3c, the Nyquist plots for each electrode contained a semicircle in the high-frequency region and a diagonal line in the low-frequency region, representing the charge transfer impedance ($R_{ct}$) and ion diffusion impedance, respectively. The results showed that the $MoS_2/NiS_2$ heterostructure had the smallest $R_{ct}$ (11.0 Ω) value than that of $NiS_2$ (33.6 Ω) and $MoS_2$ (18.6 Ω), indicating the improvement of the electrical conductivity of the heterostructure material.

In addition to EIS analysis, density functional theory (DFT) calculations also provide evidence theoretically for the enhanced conductivity of heterostructure materials. Zhang et al. [45] prepared a $Ni_3Se_4/CoSe_2$ heterostructure material. From the density of state (DOS) diagram (Figure 3d), $Ni_3Se_4/CoSe_2$ had no obvious band gap compared with pure $CoSe_2$, and the higher DOS near the Fermi level indicated that the formation of heterointerfaces enhanced the electrical conductivity. The charge density difference showed that the charges were redistributed at the heterointerfaces and the BIEFs was formed (Figure 3e), which promoted the migration of electrons and ions, giving the excellent rate and cycling performance of $Ni_3Se_4/CoSe_2$. The above studies demonstrated that the heterostructures can enhance the electrical conductivity and facilitate fast the reaction kinetics of materials.

### 3.3 Increase ion adsorption ability

When two materials come into contact, the charges around the heterointerfaces will be redistributed, causing the original neutral regions near the heterointerfaces to be ionized and assumed positive or negative charge. These regions can act as active sites, facilitating the adsorption of the oppositely charged carriers. As a result, positively charged alkali metal ions can be adsorbed in the negatively charged regions near the heterointerfaces, lowering the adsorption energy barriers. Meanwhile, the edges of the heterointerfaces and active surfaces are largely exposed, which are beneficial for the ion adsorption and redox reactions.

Fang et al. [46] investigated the effect of the $CoSe_2$/ZnSe heterointerfaces on the reaction kinetics. Differential charge density and Bader charge analysis revealed that the heterointerfaces led to the charge redistribution. The electrons migrated from the $CoSe_2$ to the ZnSe side and finally accumulated on the ZnSe side (**Figure 4**a). The charge density difference (red line) and plane average electrostatic potential (cyan line) diagrams of the $CoSe_2$/ZnSe interfaces showed that the average electrostatic potential of ZnSe was much higher than that of $CoSe_2$ (Figure 4b). This indicated that there was a strong electric field at the interfaces, which pushed electrons from the $CoSe_2$ to the ZnSe side and eventually led to the formation of electron-rich regions on the ZnSe side. $Na^+$ could be strongly adsorbed on this region (Figure 4c).

Fang et al. [47] studied the $Na^+$ storage behavior in $Sb_2S_3$/$SnS_2$ heterostructures by DFT calculations. The band gaps of $Sb_2S_3$ and $SnS_2$ semiconductors are 2.10 and 1.72 eV, respectively. When the two phases contact to form heterostructures, electrons at the two-phase interface will transfer from the $Sb_2S_3$ to the $SnS_2$ phase, resulting in the formation of electron-poor and electron-rich regions at the $Sb_2S_3$ and $SnS_2$ sides, respectively, thereby forming the BIEFs pointed from the $Sb_2S_3$ to the $SnS_2$. $Na^+$ can be strongly adsorbed on the $SnS_2$ side with low electrostatic potential to neutralize the accumulated electrons. The low $Na^+$ diffusion barriers at the $SnS_2$ side facilitated its migration, thus forming the "$Na^+$ reservoir". Although the electric field at the heterointerfaces disappeared due to the charge balance, its high $Na^+$ concentration gradient will drive $Na^+$ transport to both sides of the heterointerfaces, achieving excellent reaction kinetics.

### 3.4 Enhance structural stability

During the discharged/charged processes, different components in heterostructure materials have different redox potentials and multi-step electrochemical reactions, which stimulate the complementarity and synergy between the reactants, thereby alleviating the volumetric strain and enhancing the cycling stability of the heterostructures.

Wang et al. [48] constructed $Sb_2S_3$/$MoS_2$ heterostructures and investigated its sodium storage mechanism (Figure 4d). During the cathodic process, $Na^+$ firstly intercalated into the $MoS_2$ and formed the $Na_xMoS_2$ phase (about 1.25 V), followed by the alloying reactions of $Sb_2S_3$ to generate metallic Sb and $Na_3Sb$ (0.91 to 0.48 V). Finally, the conversion reaction occurred between the $Na_xMoS_2$ and $Na^+$ to generate the Mo phase (about 0.39 V). The uniform preformed $Na_xMoS_2$ can restrict the volume expansion of the $Sb_2S_3$ component. At the same time, the formation of Mo can also confine the disorder distribution and

volume expansion of the $Na_3Sb$. The *in-situ* XRD measurement (Figure 4e) confirmed the reaction process. The different redox potentials of the $Sb_2S_3$ and $MoS_2$ components endowed the heterostructures with smooth volume expansion during the sodiation process, enhancing the reversibility and structural stability of the material.

MXenes possess excellent electrical conductivity, flexibility and structural stability. Its two-dimensional layered structures can mitigate the volume expansion of the active materials during cycling. Therefore, constructing heterostructures between the transition metal chalcogenides and MXenes can enhance the electrochemical performance. Xu et al. [49] synthesized $MoSe_2$/MXene heterostructures by a simple hydrothermal method and subsequent thermal annealing. There were obvious phase interfaces in the $MoSe_2$/MXene heterostructures. The MXene and $MoSe_2$ were closely combined through van der Waals forces. As the conductive substrate, MXene not only greatly improved the electrical conductivity, but also alleviated the volume expansion of the $MoSe_2$ and enhanced the whole structural stability during the discharged/charged process.

**3.5 Induce more active sites**

Due to the lattice mismatch and the lattice distortion, a large number of defects will be generated at the heterointerfaces, providing more active sites for $Na^+$ adsorption. Zhao et al. [50] prepared $Bi_2S_3$-CuS heterostructures with carbon-based supports. HRTEM images showed that there were obvious heterointerfaces between the $Bi_2S_3$ and CuS phase. In addition, the generation of defects and lattice distortions was observed at the heterointerfaces. Experimental and DFT calculation results showed that the defects generated at the heterointerfaces not only provided more reactive sites for $Na^+$ adsorption, but also improved the conductivity of the material. Therefore, the defective $Bi_2S_3$-CuS/C material displayed a high discharged capacity of 645.5 mAh $g^{-1}$ at 1 A $g^{-1}$ and obtained a high reversible capacity of 592.2 mAh $g^{-1}$ after 1000 cycles at 15 A $g^{-1}$.

Furthermore, Li et al. [51] reported the $WS_2$/ZnS heterostructures with sulfur vacancies. Since the electronegativity of Zn is stronger than that of W, Zn is more easily combined with S, which led to the generation of $WS_2$/ZnS heterostructures during the synthesis process and the formation of sulfur-rich vacancies in $WS_2$ side. Sulfur vacancies can provide additional active sites for redox reactions and promote the ion diffusion.

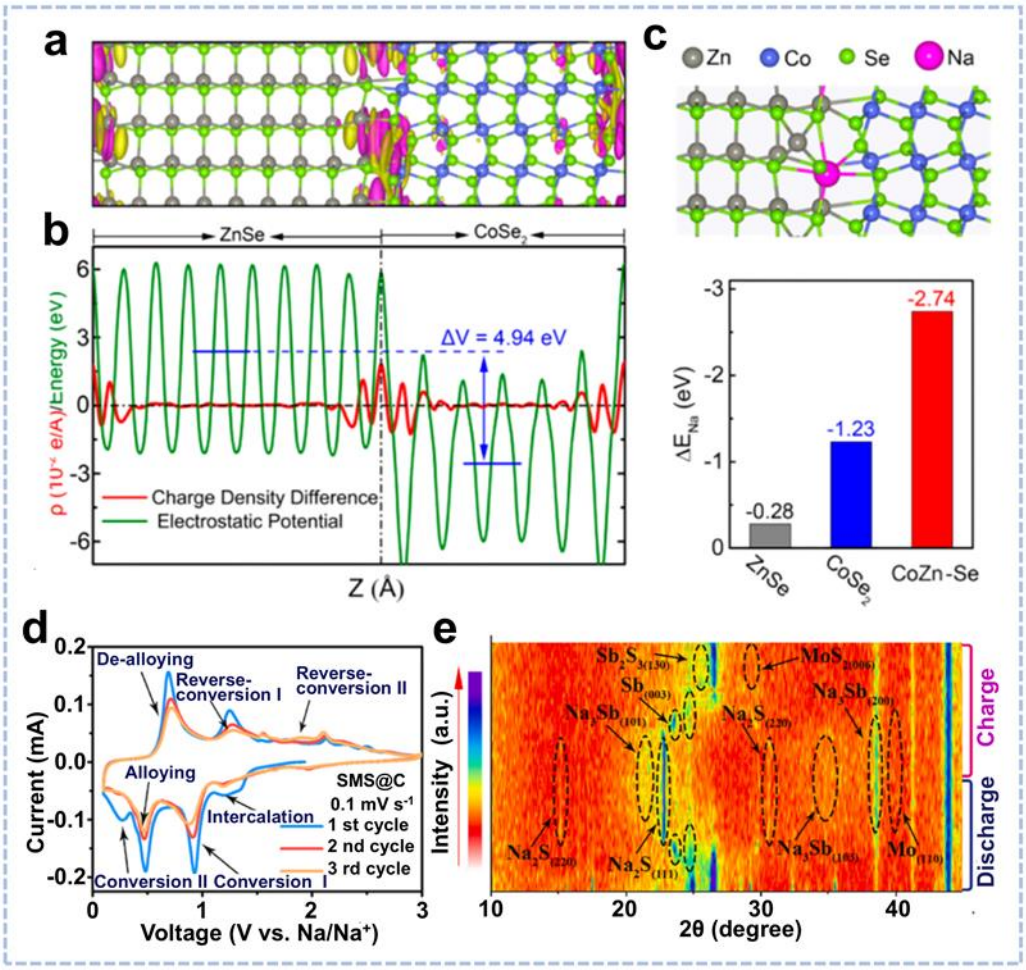


**Figure 4**. a) Charge density difference of CoZn-Se heterointerface (charge accumulation and depletion are displayed by red and yellow bubbles, respectively). b) Planar and macroscopic averaged electrostatic potential. c) Na adsorption energy. Reproduced with permission.[46]. Copyright 2019, American Chemical Society. d) CV curves of $Sb_2S_3/MoS_2$ electrode. e) *In-situ* XRD patterns of $Sb_2S_3/MoS_2$ electrode during first discharged/charged process. Reproduced with permission.[48] Copyright 2021, Elsevier.

**4. Applications of heterostructure materials in SIBs**

As mentioned above, the heterostructures formed by two-phase materials can accelerate the electron/ion migration kinetics and provide more active sites at the heterointerfaces, thus improving the reversible capacity of the materials. Meanwhile, the multi-step redox mechanisms in the heterostructures can alleviate the $Na^+$ intercalation/deintercalation stress, enhancing the structural stability and improving the long cycling performance. The rational construction of heterostructures can combine the advantages of the different single component to improve their electrochemical performances.

According to the different constructed blocks of the heterostructures. Metal chalcogenides-based heterostructures can be divided into the following main categories: metal sulfides/sulfides heterostructures, metal sulfides/oxides heterostructures, metal sulfides/selenides heterostructures, metal selenides/selenides heterostructures, metal selenides/oxides heterostructures and chalcogenides/MXene heterostructures. In this section, the recent advances of the metal chalcogenides-based heterostructure anodes for SIBs will be discussed in depth. The key electrochemical properties of various heterostructures are summarized in Table 1. The heterostructure materials demonstrate superior electrochemical performance due to the unique properties of the heterointerfaces.

**Table 1**. Summary of sodium storage performances of the various heterostructure anodes.

| Classifications | Materials | Voltage Windows [V] | ICE [%] | Cycling stability [mAh $g^{-1}$/A $g^{-1}$/cycles] | Rate capability [mAh $g^{-1}$/A $g^{-1}$] | Ref. |
|---|---|---|---|---|---|---|
| Sulfides/sulfides heterostructures | $WS_2/MoS_2/Ti_3C_2T_x$ | 0.01-3 | 65 | 245.3/2/2800 | 224.7/10 | [52] |
| | $Cu_2S$@NC@$MoS_3$ | 0.2-3 | 81 | 491/3/2000 | 424 /15 | [53] |
| | $Bi_2S_3$–CuS | 0.01-3 | 93.8 | 592.2/8/1000 | 459.9/20 | [50] |
| | d-$Co_9S_8$@$MoS_2$/S- | 0.01-3 | 80.2 | 389.7/5/500 | 398.3/10 | [54] |
| | $Fe_7S_8/FeS_2$/NCNT | 0.01-3 | 73.4 | 466.7/5/1000 | 536.5/20 | [55] |
| | H-NiS/$NiS_2$@C | 0.01-3 | 78.4 | 433/10/4500 | 509.9/2 | [56] |
| | $Co_{1-x}S$-$CoS_2$/CNF | 0.01-3 | 93.2 | 380.1/5/5000 | 495.3/10 | [57] |
| | C@$MoS_2$-$CoS_2$-O@C | 0.01-3 | 76.8 | 466.1/1/200 | 325.5/20 | [58] |
| | $MoS_2$/SnS/rGO | 0.01-3 | 56.9 | 255.4/5/500 | 325.2/10 | [59] |
| | $Cu_2S$@ZnS/C | 0.4-2.6 | 93.5 | 379/2/1000 | 352/10 | [60] |
| | $CoS_2/NiS_2$ | 0.3-3 | 88.4 | 545.1/5/2000 | 541.7/5 | [61] |
| | $MoS_2$/SnS@C | 0.01-3 | — | 292/5/2000 | 325/15 | [62] |
| | CuS/$FeS_2$@NC | 0.01-2.7 | — | 563/2/300 | 199/10 | [63] |
| | $VS_4/Bi_2S_3$@C | 0.05-2.5 | 79.4 | 379/2/1800 | 410.8/5 | [64] |
| | $MoS_2/NiS_2$ | 0.2-3 | 86 | 480.5/1/350 | 339.4/10 | [65] |
| | $MoS_2$-$ZnIn_2S_4$ | 0.01-3 | 89.3 | 455.9/4/1000 | 474.3/20 | [66] |
| | $Sb_2S_3/MoS_2$ | 0.1-3 | 79.5 | 411.5/5/650 | 408.7/10 | [48] |
| | FeS/NiS | 0.01-3 | 62 | 431/0.1/100 | 315/1.6 | [67] |
| | $Fe_9S_{10}$@$MoS_2$@C | 0.01-3 | 80.1 | 355/2/1000 | 197/30 | [43] |
| | $Cu_2S/MoS_2$⊂PCF | 0.2-3 | 94.4 | 245.2/4/800 | 260.2/10 | [68] |
| | $WS_{2-x}$/ZnS@C | 0.01-3 | — | 170.8/5/5000 | 191.9/20 | [51] |

| | | | | | | |
|---|---|---|---|---|---|---|
| | $Bi_2S_3$@$Co_9S_8$ CHPs | 0.01-3 | 77 | 595/0.5/800 | 432/5 | [69] |
| | $Bi_2S_3$/$MoS_2$ | 0.1-3 | 81.5 | 323/10/1200 | 325.5/10 | [70] |
| | $Sb_2S_3$@$FeS_2$ | 0.1-3 | 82.4 | 534.8/5/1000 | 537.9/10 | [71] |
| | $MoO_3$-$MoS_2$ | 0.01-3 | 59.8 | 286/5/2300 | 316/10 | [72] |
| | $VS_2$/$VO_x$ | 0.3-3 | 90 | 721.6/2/1000 | 654.8/10 | [73] |
| | $MoO_2$/$MoS_2$@NSC | 0.1-3 | 66 | 260/5/390 | 347/5 | [74] |
| Sulfides/oxides | SnS/$Fe_2O_3$-G | 0.01-3 | 82.7 | 386.5/2/2000 | 399.2/10 | [75] |
| heterostructures | 1T-$MoS_2$/$MoO_x$ | 0.01-3 | 78.2 | 473.8/2/1300 | 74.94/1 | [76] |
| | $FeS_2$/$Fe_2O_3$@N- | 0.01-3 | 62.9 | 287/1/600 | 246.2/3.2 | [77] |
| | 1T/2H $MoS_2$@$SnO_2$ | 0.01-3 | 45.7 | 262/2/500 | 114/5 | [78] |
| | $MoS_2$@$MoO_2$-C | 0.01-3 | 74 | 400/5/6000 | 398/10 | [79] |
| | $V_{1.11}S_2$/$V_{1.13}Se_2$/C | 0.01-3 | — | 553/10/1000 | — | [80] |
| Sulfides/selenides | $CoS_{2-x}Se_x$@SG | 0.4-3 | 95.5 | 542.6/5/1000 | 412.8/30 | [81] |
| heterostructures | $NiS_2$/$NiSe_2$ | 0.01-3 | 97.4 | 405/2/1500 | 353/5 | [82] |
| | SnS/$SnSe_2$ | 0.01-3 | 55.2 | 580/0.1/100 | 267/10 | [83] |
| | $SnSe_2$/$NiSe_2$@NC | 0.3-3 | 83.4 | 322.7/3/7500 | 314.6/10 | [84] |
| | $Ni_3Se_4$/$CoSe_2$@C | 0.01-2.8 | 83.8 | 355/2.5/500 | 321.9/10 | [45] |
| | $Ni_3Se_4$/$CoSe_2$ | 0.01-3 | 54.5 | 243/1/600 | 206/3 | [85] |
| | $FeSe_2$/$Fe_3Se_4$ | 0.01-3 | 95.9 | 208.8/8/2000 | 297.2/5 | [37] |
| Selenides/selenides | $CoSe_2$-$Cu_2Se$@NC | 0.01-3 | — | 415/20/2000 | 480/25 | [86] |
| heterostructures | $CoSe_2$/ZnSe@NC | 0.01-3 | 71.7 | 232/10/3000 | 244.8/10 | [87] |
| | $Fe_3Se_4$/ZnSe@C | 0.01-3 | — | 473.8/5/300 | 412.5/5 | [88] |
| | $In_2Se_3$-$CoIn_2$-$CoSe_2$ | 0.01-2.5 | 61.2 | 297.5/5/2000 | 371.6/20 | [89] |
| | $SnSe_2$/ZnSe@PDA | 0.1-3 | 71.6 | 616/1/1000 | 253.3/4 | [90] |
| | ZnSe/2($CoSe_2$)@N | 0.01-3 | 62.7 | 552/0.1/100 | 528.6/5 | [91] |
| Selenides/oxides | $V_{1.13}Se_2$/$V_2O_3$ | 0.01-3 | 94 | 328.5/2/1500 | 278.9/5 | [92] |
| heterostructures | $SnO_2$/$SnSe_2$@C | 0.01-3 | 69.5 | 351/2/1000 | 322/4 | [93] |
| | g-$MoO_2$@s-$MoSe_2$ | 0.01-3 | 57.8 | 254.2/5/6000 | 245.3/10 | [94] |
| | MXene-$MoS_2$ | 0.01-3 | 63 | 220/2/1000 | 146/10 | [95] |
| | $Ti_3C_2T_x$/$FeS_2$ | 0.01-3 | 86 | 474.9/5/600 | 456.6/10 | [96] |
| Chalcogenides/MXen | $SnS_2$ QDs/$Ti_3C_2$ | 0.01-3 | 55.1 | 345/0.1/600 | — | [97] |
| e heterostructures | $Fe_{x-1}Se_x$/MXene | 0.01-3 | 52.4 | 348/10/2000 | 453.1/5 | [98] |
| | $Cu_{1.75}$Se-MXene | 0.01-3 | 58.4 | 480.7/1/1000 | 355.3/5 | [99] |
| | $MoSe_2$/MXene | 0.1-3 | 69.9 | 384/2/400 | 250/10 | [49] |

### 4.1 Metal sulfides/sulfides heterostructures

Metal sulfides have high theoretical capacities. The weak M-S bonds make them highly reversible during the conversion reactions, thus metal sulfides usually have high initial Coulombic efficiencies (ICE). However, metal sulfides still face problems such as slow electron/ion migration kinetics and large volume expansion during the discharged/charged process.[100] Compared with single metal sulfides, the

heterostructures constructed by coupling the two metal sulfides with different band gaps can induce the generation of the BIEFs, reducing the internal resistances, promoting the electrode reaction kinetics and improving the electrochemical performance.

Cheng et al. [66] prepared $MoS_2$@$ZnIn_2S_4$ heterostructures. The effect of the heterostructures on the electrochemical properties was studied by DFT calculation. According to the difference in crystal structures, $ZnIn_2S_4$ and $MoS_2$ can form two different heterointerfaces. One is the heterointerface formed by the Zn surface in $ZnIn_2S_4$ and $MoS_2$ ($MoS_2$-$ZnIn_2S_4$), and another is formed by the In surface in $ZnIn_2S_4$ and $MoS_2$ ($MoS_2$-$ZnIn_2S_4$*), respectively. The DOS results indicated that the formation of the above heterostructures enhanced the electrical conductivity. At the $MoS_2$-$ZnIn_2S_4$ interfaces, the calculated work function value of $ZnIn_2S_4$ (6.11eV) was higher than that of $MoS_2$ (5.18eV) (**Figure 5**a). Electrons flowed from $MoS_2$ to the $ZnIn_2S_4$ side, resulting in the formation of positive and negative charged spaces on the $MoS_2$ and $ZnIn_2S_4$ sides, respectively, thereby forming the BIEFs pointed from $ZnIn_2S_4$ to $MoS_2$. The BIEFs generated additional electromotive force and promoted electron transfer. The differential charge density also confirmed this result (Figure 5c). Additionally, at the $MoS_2$-$ZnIn_2S_4$* interfaces, electrons transferred from the $ZnIn_2S_4$ to the $MoS_2$. And the direction of the BIEFs was opposite to that of $MoS_2$-$ZnIn_2S_4$ interfaces (Figure 5b, d). The DFT calculation results showed that $Na^+$ had the lowest diffusion energy barriers at the heterointerfaces. Heterostructure materials possessed high reactivity and fast electron/ion diffusion kinetics. Based on the CV (Figure 5e) and in-situ XRD results (Figure 5f), the reaction mechanism of $MoS_2$@$ZnIn_2S_4$ heterostructures during the redox process was as follows.

Discharged process:

$$MoS_2 + xNa^+ + xe^- \rightarrow Na_xMoS_2\ (\approx 1.55\ V) \quad (1)$$

$$ZnIn_2S_4 + xNa^+ + xe^- \rightarrow Na_xZnIn_2S_4\ (\approx 0.90\ V) \quad (2)$$

$$3Na_xZnIn_2S_4 + (10\text{-}3x)Na^+ + (10\text{-}3x)e^- \rightarrow 5Na_2S + In_6S_7 + 3Zn\ (\approx 0.40\ V) \quad (3)$$

$$Na_xMoS_2 + (4\text{-}x)Na^+ + (4\text{-}x)e^- \rightarrow 5Na_2S + Mo\ (\approx 0.37\ V) \quad (4)$$

Charged process:

$$5Na_2S + In_6S_7 + 3Zn \rightarrow 3ZnIn_2S_4 + 10Na^+ + 10e^-\ (\approx 0.5\text{-}1.20\ V) \quad (5)$$

$$Mo + 2Na_2S \rightarrow MoS_2 + 4Na^+ + 4e^-\ (\approx 1.56\ V) \quad (6)$$

The stepwise intercalation conversion reaction mechanism of $MoS_2$ and $ZnIn_2S_4$ provided the synergistic effect to alleviate the degradation of the material during the whole electrochemical process. Therefore, the $MoS_2$@$ZnIn_2S_4$ heterostructures exhibited

excellent rate capability (Figure 5g) and cycling stability with discharged capacity of 455.9 mAh $g^{-1}$ after 1000 cycles at 4 A $g^{-1}$.

The construction of bimetallic sulfide heterostructures can improve the reaction kinetics and optimize the electrochemical performance. However, there still lack thorough understanding of the reaction mechanisms at the highly active phase interfaces existed between the different phases of the heterostructures. Fan et al. [64] prepared carbon-coated $VS_4/Bi_2S_3$@C heterostructures by hydrothermal method and subsequent sulfurization treatment process. The $VS_4/Bi_2S_3$@C heterostructures exhibited nanorod-like morphology and obvious phase interfaces. As evidenced by *in-situ* XRD results (Figure 5h), the heterostructures underwent multi-step redox reactions during the discharged/charged process. The intercalation, conversion and alloying reactions steeply occurred during the discharging process, eventually generating V, $Na_xBi$, and $Na_2S$. During the charging process, $VS_4$ and $Bi_2S_3$ phases reappeared, indicating the excellent reversibility of this heterostructures. Meanwhile, ex-situ TEM results confirmed that the recrystallization process can produce rich phase boundaries between the heterointerfaces during cycling and the $VS_4/Bi_2S_3$@C heterostructures still maintained excellent structural integrity. According to the experiments and DFT calculations, the heterostructures had strong interfacial interactions and significantly enhanced the electrical conductivity, while the BIEFs formed at the phase interfaces can further enhance the reaction kinetics of $Na^+$. This material exhibited excellent cycle performance (capacity of 379.0 mAh $g^{-1}$ at 2 A $g^{-1}$ for 1800 cycles).

High-performance metal sulfide anodes still face problems in practical application such as slow electrochemical kinetics and large volume expansion during the discharged/charged process. The construction of heterostructures could solve these problems. Je et al.[63] prepared the $CuS/FeS_2$ heterostructure homogeneously distributed in a nitrogen-doped carbon framework ($CuS/FeS_2$@NC). FE-SEM images showed that the morphology of $CuS/FeS_2$@NC was nanocubes and the particle size ranged from about 500-600 nm. The nitrogen-doped porous carbon not only improved the ion/electron transport, but also alleviated the volume expansion and enhanced the structural stability of the active materials during the redox process. Meanwhile, the introduction of CuS with high conductivity into the heterostructures accelerated the $Na^+$ and electron transport kinetics. Therefore, the $CuS/FeS_2$@NC anode provided excellent cycling stability (Figure 5i). By a similar method, researchers have prepared several PBA-derived bimetallic

sulfides such as NiS/FeS[67], $NiS_2$@$CoS_2$[101]. The electrochemical performance of these metal sulfides enhanced greatly in SIBs.

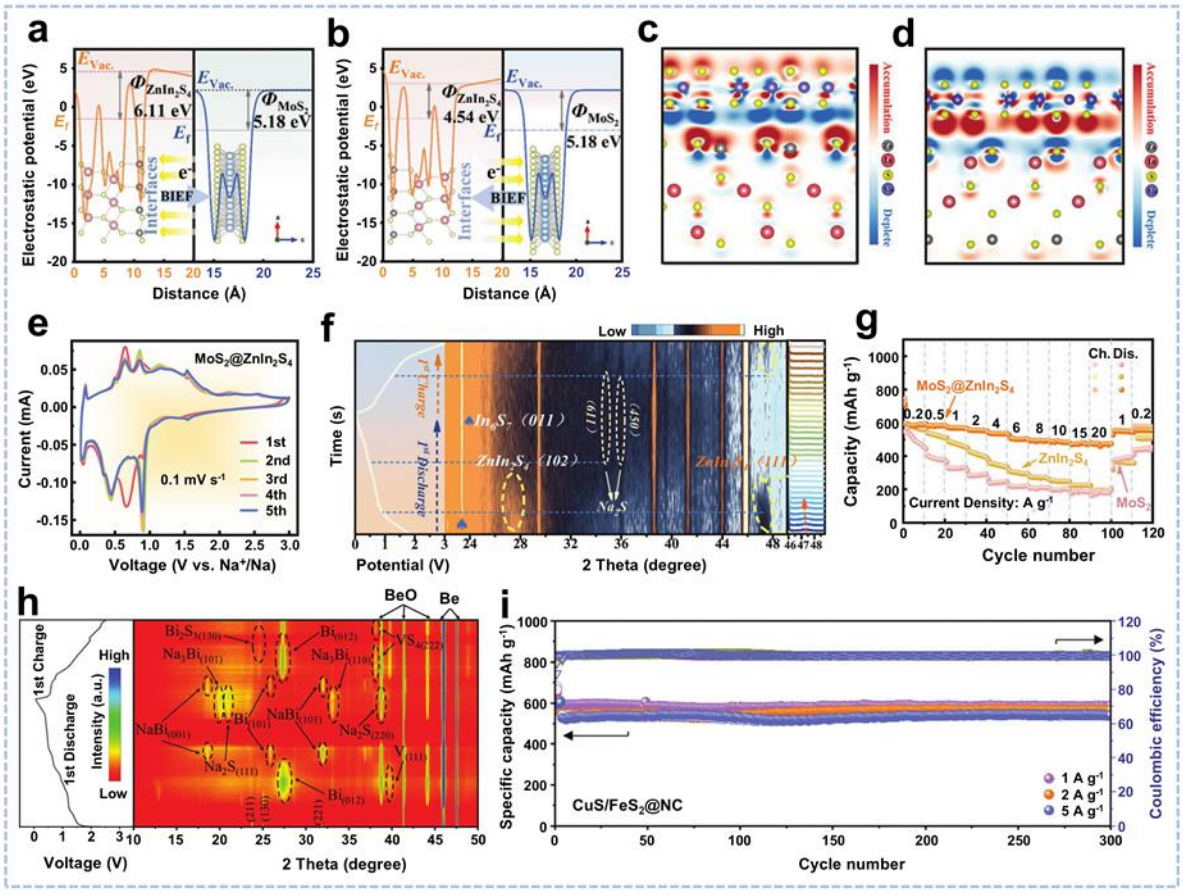


**Figure 5.** Electrostatic potentials of: a) $MoS_2$-$ZnIn_2S_4$ and b) $MoS_2$-$ZnIn_2S_4$*. Charge density differences of: c) $MoS_2$-$ZnIn_2S_4$ and d) $MoS_2$-$ZnIn_2S_4$*. e) CV curves, f) *In-situ* XRD patterns during the first cycle and g) Rate capability of $MoS_2$-$ZnIn_2S_4$ electrode. Reproduced with permission.[66] Copyright 2022, Wiley-VCH. h) *In-situ* XRD patterns of $VS_4$/$Bi_2S_3$@C electrode during the initial cycle. Reproduced with permission.[64] Copyright 2022, Wiley-VCH. i) Cycling performance of CuS/$FeS_2$@NC at various current densities. Reproduced with permission.[63] Copyright 2022, Wiley-VCH.

### 4.2 Metal sulfides/oxides heterostructures

Compared with metal sulfides, metal oxides have superior chemical stability and could act as protective layers to alleviate the volume expansion of the metal sulfides during the discharged/charged process. Therefore, designing metal sulfide/oxide heterostructure materials has attracted widespread attention. Zhang et al. [73] constructed $VS_2$/$VO_x$ heterostructures based on the spontaneous hydrolysis and oxidation reaction of $VS_2$ in water (**Figure 6**a). The formation of the heterostructures mainly included two processes: the hydrolysis process of the $VS_2$, followed by the oxidation reaction to form

$VO_x$ layer on the surface of $VS_2$. The components of $VO_x$ were mainly $VO_2$, $V_6O_{13}$ and $V_2O_5$ (Figure 6b). Thanks to the high electrical conductivity of $VS_2$ and the high chemical stability of $VO_x$, the as-prepared $VS_2/VO_x$ electrode exhibited excellent rate capability (up to 654.8 mAh $g^{-1}$ at 10 A $g^{-1}$) (Figure 6c) and superior cycling performance (up to 721.6 mAh $g^{-1}$ after 1000 cycles at 2 A $g^{-1}$). Theoretical calculations showed that this heterostructures reduced the energy barrier of Na migration and increased the electrical conductivity of $VS_2/VO_x$ electrode.

$MoS_2$ possesses the graphite-like two-dimensional layered structure with an interlayer distance of 0.62 nm and displays high theoretical capacity (670 mAh $g^{-1}$) via multi-electron redox reaction. However, the large volume expansion of $MoS_2$ nanosheets during the discharged/charged process leads to the decay of electrochemical properties.[102-104] Yu et al.[72] prepared nanorod-shaped $MoO_3$-$MoS_2$ heterostructures. There was obvious charge transfer at the heterostructure surface (Figure 6d), the formation of BIEFs and the generation of amorphous and defective regions were conducive to improving the transfer kinetics of ions and electrons. In addition, the heterostructures restricted the volume expansion of the material and enhanced the structural stability. The results of CV (Figure 6e) and *in-situ* XRD test (Figure 6f) showed that $MoO_3$-$MoS_2$ exhibited an intercalation-conversion charge storage mechanism, which endowed $MoO_3$-$MoS_2$ with high specific capacity. In addition, the $MoO_3$-$MoS_2$ also exhibited excellent rate performance (316 mA h $g^{-1}$ at 10 A $g^{-1}$) and long-term cycle stability (286 mA h $g^{-1}$ after 2300 cycles at 5 A $g^{-1}$).

SnS possesses layered structure (interlayer distance: 4.3 Å) and high theoretical capacity (1022 mAh $g^{-1}$). Nevertheless, its severe volume expansion leads to comminution of the structure, thus causing rapid capacity fading during the redox process [105, 106]. In addition, the sluggish reaction kinetics and relatively poor conductivity of SnS lead to poor rate capability. To address these issues, Cheng et al. [75] firmly anchored the $SnS/Fe_2O_3$ heterostructures on a few-layer graphene to construct the $SnS/Fe_2O_3$-G heterostructures (Figure 6g). The BIEFs formed between the two phases lowered the $Na^+$ migration barrier and enhanced $Na^+$ diffusion/adsorption kinetics. At the same time, graphene can be used as a conductive buffer layer to further alleviate the volume expansion of the active materials and improve their cycling stability. Consequently, the $SnS/Fe_2O_3$-G heterostructures exhibited ultrahigh cycling life (up to 442.2/386.5 mAh $g^{-1}$ after 2000 cycles at 1/2 A $g^{-1}$).

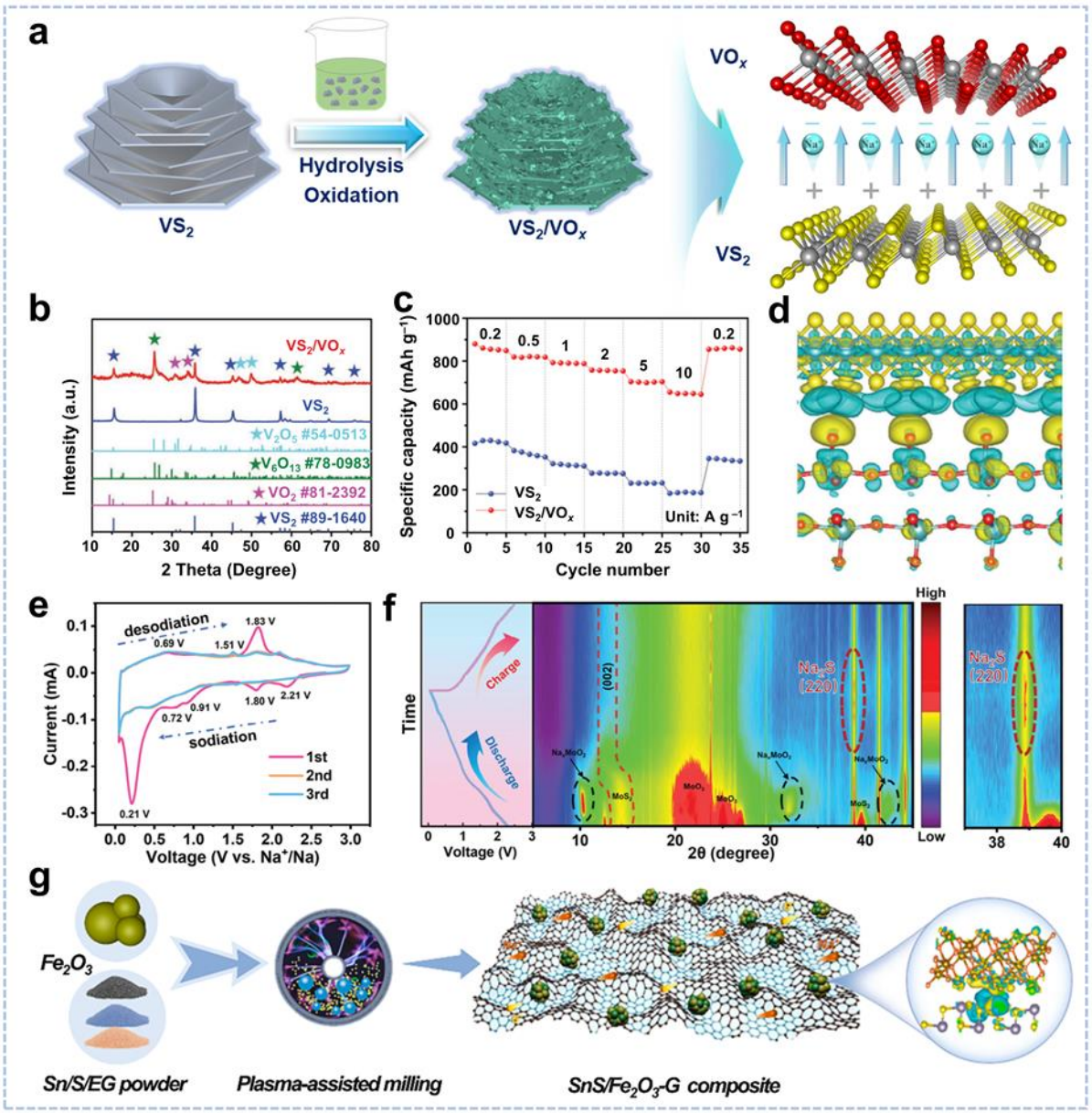


**Figure 6.** a) Schematic diagram of the preparation of $VS_2/VO_x$ heterostructures. b) XRD patterns, c) Rate performance of $VS_2/VO_x$ heterostructures. Reproduced with permission.[73] Copyright 2023, Wiley-VCH. d) Differential charge density diagram of $MoO_3$-$MoS_2$ heterointerface. e) CV curves of $MoO_3$-$MoS_2$ electrode at 0.1 mV $s^{-1}$. f) *In-situ* XRD evolution profiles of $MoO_3$-$MoS_2$ electrode for first discharged/charged process. Reproduced with permission.[72] Copyright 2024, Wiley-VCH. g) Schematic diagram of the preparation of $SnS/Fe_2O_3$-G at 1/2 A $g^{-1}$. Reproduced with permission.[75] Copyright 2023, Elsevier.

### 4.3 Metal sulfides/selenides heterostructures

Metal selenides have excellent electrical conductivity. In addition, compared with oxygen and sulfur, selenium has larger atomic radius. Therefore, the metal selenide bonds

are relatively easy to break, which could accelerate the conversion reaction kinetics [90]. Therefore, constructing the metal sulfides/selenides heterostructures could improve the electrochemical properties of the materials.

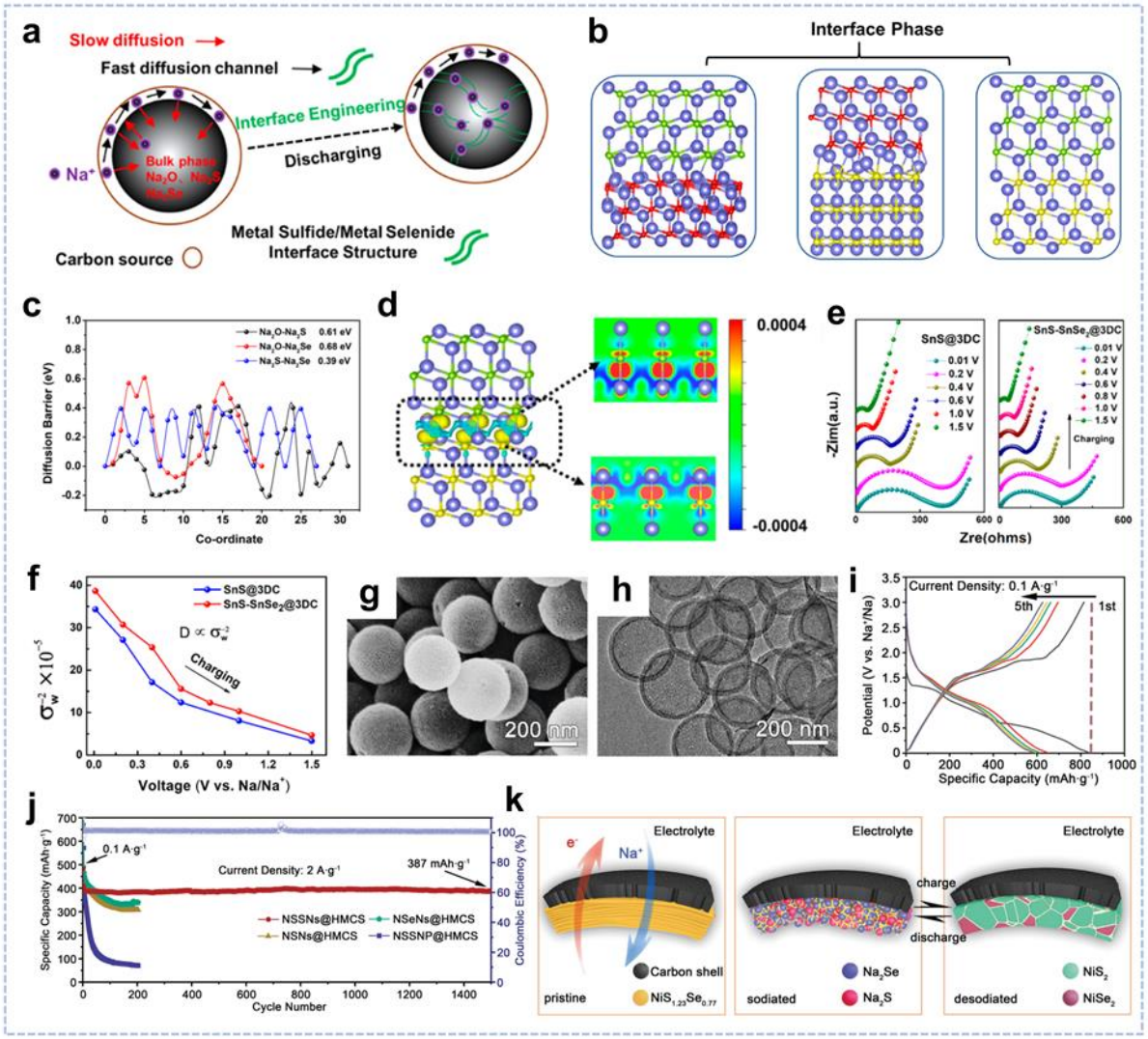


**Figure 7.** a) The illustration for the interface engineering. b) The optimized structures of the $Na_2O/Na_2Se$, $Na_2O/Na_2S$, and $Na_2S/Na_2Se$ interfaces. c) Na atom migration energy barriers in three interface structures. d) Charge density difference of $Na_2S/Na_2Se$ interface. e) EIS curves at different cut-off voltages of the SnS@3DC and SnS-$SnSe_2$@3DC electrodes. f) Diffusion coefficients calculated at different cut-off voltages for the SnS-$SnSe_2$@3DC electrode. Reproduced with permission.[83] Copyright 2020, American Chemical Society. g) SEM and h) TEM images of NSSNs@HMCS. i) Discharge/charge profiles of NSSNs@HMCS electrode. j) Cycling performance at 2 A $g^{-1}$. k) Schematic diagram of the evolution of electrode morphology during discharged/charged process. Reproduced with permission.[82] Copyright 2021, Wiley-VCH.

The diffusion of $Na^+$ in the discharged bulk products ($Na_2O$, $Na_2S$, and $Na_2Se$) of the composites (graphene/metal oxides, sulfides, selenides) is slow (**Figure 7**a). Wang et al. [83] systematically studied the $Na^+$ diffusion behavior in different discharged products ($Na_2O/Na_2S$, $Na_2O/Na_2Se$ and $Na_2S/Na_2Se$) of the various heterostructures. The three optimized interface models are shown in Figure 7b. The $Na_2S/Na_2Se$ heterointerface displayed minimal structural distortion, while Na atoms in both $Na_2O/Na_2S$ and $Na_2O/Na_2Se$ heterointerfaces exhibited partial aggregation. Meanwhile, the $Na_2S/Na_2Se$ heterointerfaces had the strongest interfacial strength and the lowest $Na^+$ migration energy barrier (Figure 7c). Clear electron exchange was observed in the region of the heterointerfaces (Figure 7d). Based on the theoretical analysis, the $SnS/SnSe_2$@3DC heterostructure was synthesized. Experimental results showed that the $SnS/SnSe_2$@3DC heterostructure exhibited excellent rate performance as the SIB anode. The $SnS/SnSe_2$@3DC electrode had lower internal resistance and larger ion diffusion coefficient than the SnS@3DC electrode (Figure 7e, f), delivering superior electrochemical performance.

Although heterostructure engineering has successfully improved the sodium storage performance of the electrode materials, the increase of phase interfaces in heterostructures may introduce additional side reactions, leading to low ICE and inferior cycling life of the heterostructure electrodes. To address the issue, He et al. [82] reported the $NiS_{1.23}Se_{0.77}$ nanosheets encapsulated in hollow mesoporous carbon spheres (NSSNs@HMCS) (Figure 7g, h). The $NiS_{1.23}Se_{0.77}$ nanosheets transformed into $NaS_2/NaSe_2$ after first discharged process and then turned into $NiS_2/NiSe_2$ heterostructure after full charged (Figure 7k). The rich heterointerfaces of $NiS_2/NiSe_2$ lowered the $Na^+$ diffusion barrier and improved the electrode reaction kinetics. Furthermore, the $NiS_2/NiSe_2$ heterostructure reduced the dissolution of polysulfides or polyselenides and alleviated the irreversible decomposition of $Na_2S$ or $Na_2Se$ during cycling, resulting in ultrahigh ICE of 95.1% (Figure 7i) and long cycling life. On the other hand, the hollow mesoporous carbon spheres improved the electrical conductivity, alleviated the volume expansion and prevented the comminution and aggregation of the electrode material during the cycling, thus further improving the cycling stability. Consequently, the NSSN@HMCS anode exhibited excellent rate capability (428 mAh $g^{-1}$ at 5 A $g^{-1}$) and cycling stability (405 mAh $g^{-1}$ maintained after 1500 cycles at 2 A $g^{-1}$ with a capacity retention rate of 95.6%) (Figure 7j).

### 4.4 Metal selenides/selenides heterostructures

Metal selenides have narrow band gaps, thus exhibiting higher electrical conductivity than metal oxides and metal sulfides. Furthermore, the weaker M-Se bonds in metal selenides may kinetically favor the conversion reaction compared to metal oxides and sulfides[89, 107-109]. The discharged product ($Na_2Se$) of metal selenides also provides better conductivity than $Na_2O$ and $Na_2S$. Therefore, transition metal selenides are regarded as promising anode materials for SIBs. However, the fast capacity fading of metal selenides due to the large volume expansion during the conversion process greatly hinders their practical applications [110, 111]. Constructing binary selenide heterostructures with two materials with different band gaps can effectively improve the single-component $Na^+$ storage capacity and ease the volume expansion during the discharged/charged process, thereby promoting the electrode reaction kinetics and electrochemical properties of the materials[112].

$CoSe_2$ is a prospective anode material for SIBs, which has the advantages of high theoretical capacity, narrow band gap, stable chemical properties and environmental friendliness [113, 114]. However, like other selenides, it still has thorny problems such as slow $Na^+$ diffusion kinetics and large volume change during the redox process, leading to degraded electrochemical performance[115, 116]. Liu et al. [86] prepared $CoSe_2$-$Cu_2Se$ heterostructure nanospheres coated with nitrogen-doped carbon layers ($CoSe_2$-$Cu_2Se$@NC). The sodium storage mechanism was investigated by *in-situ*/*ex-situ* XRD and *ex-situ* HRTEM. The reaction mechanism of $CoSe_2$-$Cu_2Se$@NC heterostructures during discharged process was as follows:

$$CoSe_2 + xNa^+ + xe^- \leftrightarrow Na_xCoSe_2$$

$$Cu_2Se \rightarrow Cu_{2-x}Se + xCu$$

$$Na_xCoSe_2 + (4 - x)Na^+ + (4 - x)e^- \leftrightarrow Co + 2Na_2Se$$

$$Cu_{2-x}Se + 2Na^+ + 2e^- \leftrightarrow (2 - x)Cu + Na_2Se$$

After fully discharged, metallic Co, Cu, and $Na_2Se$ were generated. The formed metallic copper can act as the conductive agent for the subsequent reactions and suppress the volume expansion of $CoSe_2$ during the subsequent sodiation process. After fully charged, the $CoSe_2$-$Cu_2Se$@NC heterostructure was regenerated. The crystal phase transition mechanism of $CoSe_2$-$Cu_2Se$ during the sodiation/desodiation process was further investigated (**Figure 8**a). Reaction kinetics and DFT calculations revealed that the heterostructure facilitated the electron/ion transport and provided more active sites. The

nitrogen-doped carbon layer suppressed the agglomeration and volume expansion of the active materials as well as improved the structural integrity during the reaction process. Therefore, the $CoSe_2$-$Cu_2Se$@NC heterostructure nanospheres exhibited excellent electrochemical performance, especially the long-term cycling stability (415.1/367 mA h $g^{-1}$ maintained after 2000 cycles at 10/20 A $g^{-1}$, respectively). Zhang et al. [45] synthesized carbon-coated $Ni_3Se_4$/$CoSe_2$ heterostructures by a simple hydrothermal and annealing method. The carbon coating alleviated the volume expansion and enhanced the structural integrity of the material. The $Ni_3Se_4$/$CoSe_2$ heterostructures induced the BIEFs to promote the transport kinetics of ions/electrons during cycling. Therefore, the electrode exhibited outstanding cycling performance and rate capability (Figure 8b). Furthermore, the researchers also constructed the $In_2Se_3$-$CoIn_2$-$CoSe_2$ heterostructures with $In_2Se_3$-$CoIn_2$ and $CoSe_2$-$CoIn_2$ bilateral interfaces to optimize the sodium storage performance of $CoSe_2$, as shown in Figure 8c[89].

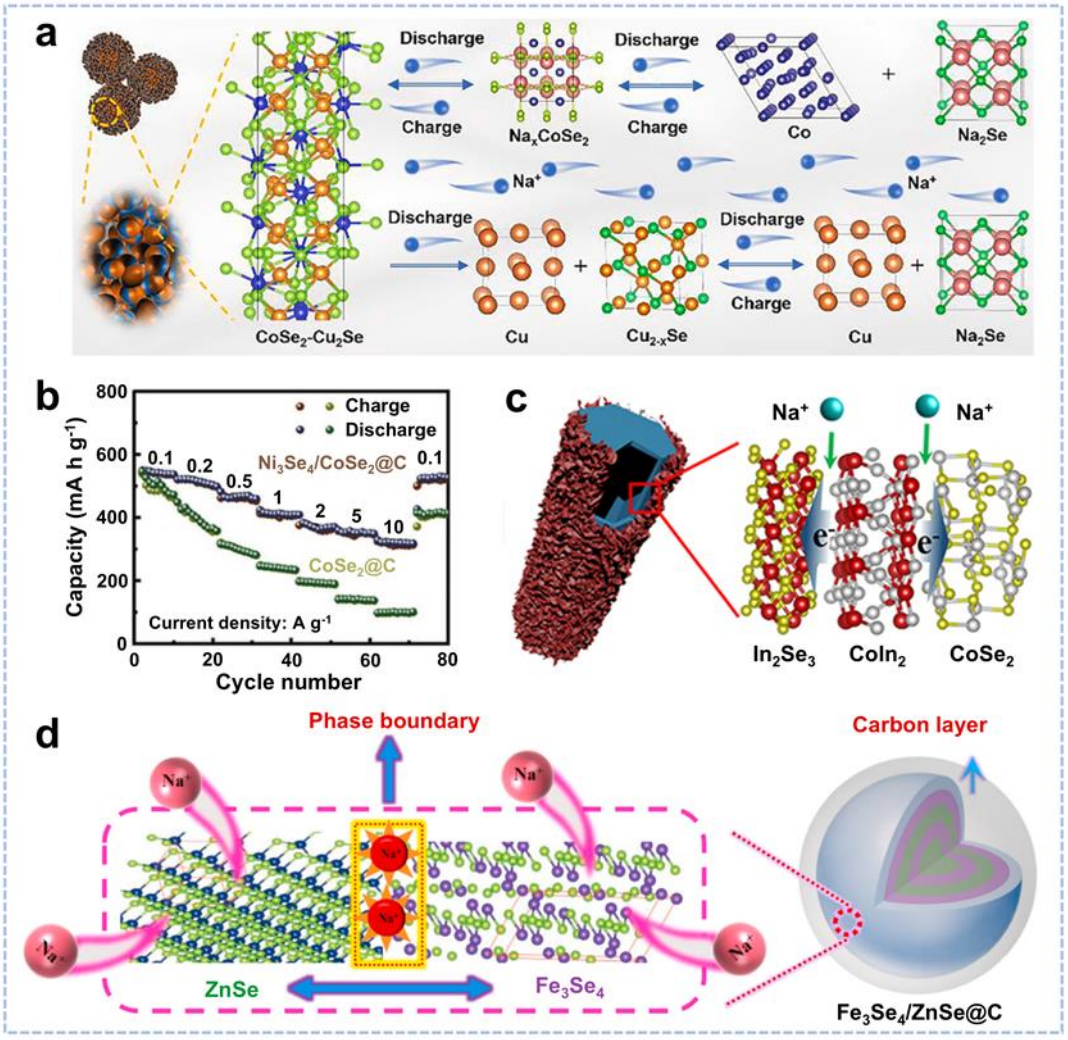


**Figure 8.** a) Schematic representation of the crystallographic phase change mechanism of $CoSe_2$-$Cu_2Se$ during sodiation/desodiation process. Reproduced with permission.[86]

Copyright 2022, Elsevier. b) Rate capabilities of $Ni_3Se_4/CoSe_2$@C for SIBs. Reproduced with permission.[45] Copyright 2022, Wiley-VCH. c) Schematic illustration of the $In_2Se_3/CoSe_2$ heterostructures. Reproduced with permission.[89] Copyright 2021, American Chemical Society. d) The schematic diagram of $Fe_3Se_4$/ZnSe@C. Reproduced with permission.[88] Copyright 2021, Elsevier.

Iron selenide has emerged as a research hotspot owing to its high theoretical specific capacity, but it still faces problems such as slow kinetics and poor cycling performance [117]. Zhang et al. [88] prepared $Fe_3Se_4$/ZnSe@C heterostructure materials with core-shell structure by solvothermal method and subsequent high-temperature selenization treatment. The heterointerfaces facilitated the charge transport and effectively enhanced the reaction kinetics. Secondly, the carbon shell maintained the structural stability of the material (Figure 8d). Consequently, the electrode showed excellent cycling stability (473.8 mAh $g^{-1}$ can maintain after 300 cycles at 5 A $g^{-1}$). Liu et al. [118] constructed a unique $Fe_3Se_4$/FeSe heterostructures with the same cations and anions. DFT calculation results showed that the heterointerfaces significantly improved the conductivity, $Na^+$ diffusion and structural stability of the material. This heterostructure anodes exhibited higher rate performance and cycling stability. In addition, Kong et al. [37] also synthesized Ni-doped $FeSe_2/Fe_3Se_4$ porous heterostructure composite embedded in Se-doped carbon framework. The synergistic effect between the heterostructures of the composite endowed the material with excellent sodium storage performance.

### 4.5 Metal selenides/oxides heterostructures

In addition to constructing appealing heterostructures, researchers have also conducted extensive research on metal selenides/oxides heterostructures[119].

The layered structure of $SnSe_2$ has large interlayer spacings (0.61 nm), and the interlayers are connected together by weak van der Waals interactions, which can provide large $Na^+$ transport channels and good electrical conductivity. In addition, $SnSe_2$ has high theoretical capacity (756 mAh $g^{-1}$). However, the large volume expansion of $SnSe_2$ during cycling seriously affects its cycling stability [120, 121]. Li et al. [93] prepared $SnO_2/SnSe_2$ heterostructure nanomaterial embedded in N-doped carbon nanotubes ($SnO_2/SnSe_2$@C). The final morphology of the $SnO_2/SnSe_2$@C heterostructure was the hollow nanotubes. The band gaps of $SnO_2$ and $SnSe_2$ are 3.8 and 1.0 eV, respectively. When the two phases come into contact, the BIEFs is induced pointing from the $SnO_2$ to $SnSe_2$. During the discharged process, the BIEFs accelerated the $Na^+$ diffusion from $SnO_2$ to the surface of

$SnSe_2$. During the charged process, since it is more difficult to extract $Na^+$ from $Na_2O$ than $Na_2Se$, $Na^+$-rich and $Na^+$-poor regions formed in the $SnSe_2$ and $SnO_2$ phase, respectively. The difference in $Na^+$ concentration induced a reverse electric field pointed from the $SnSe_2$ to $SnO_2$, thereby accelerated the extraction of $Na^+$ during the charged process (**Figure 9**a). In addition, the hollow nanotubes provided sufficient space for the volume expansion of the active materials. Thanks to the synergistic effect of the composite materials, this material exhibited great cycling performance with a capacity retention of 87.7% after 1000 cycles at 2 A $g^{-1}$.

Compared with $SnSe_2$, $MoSe_2$ also has larger interlayer spacing (0.68 nm), exhibiting structural advantages applied as electrode material for SIBs. However, similar to $MoS_2$, $MoSe_2$ nanosheets with high surface energy inevitably undergo aggregation and structural collapse during cycling, leading to the loss of active sites and deterioration of the electrochemical performance. Zeng et al. [94] prepared a b-NC/g-$MoO_2$@s-$MoSe_2$-10 heterostructure material using a tunable surface selenization route (Figure 9b). This design significantly enhanced $Na^+$ storage, improved electrode reaction kinetics and maintained the structural stability of the active material (Figure 9c). Therefore, the b-NC/g-$MoO_2$@s-$MoSe_2$-10 electrode maintained ultra-long cycling stability (capacity retention was about 89.0% after 6000 cycles at 5.0 A $g^{-1}$).

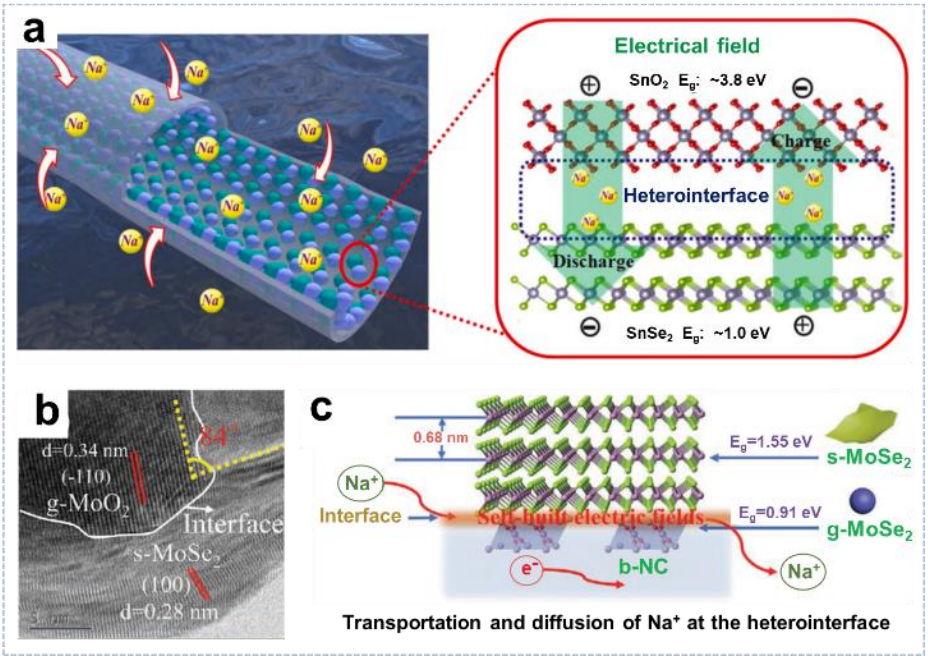


**Figure 9.** a) Schematic diagram of the enhanced sodium storage performance of $SnO_2$/$SnSe_2$@C heterostructure. Reproduced with permission.[93] Copyright 2021, Elsevier. b) HRTEM image of b-NC/g-$MoO_2$@s-$MoSe_2$-10 heterostructure. c) Schematic

diagram of $Na^+$ transport and diffusion at $MoO_2$@$MoSe_2$ heterointerface. Reproduced with permission.[94] Copyright 2020, Wiley-VCH.

### 4.6. Chalcogenides/MXene heterostructures

Transition metal carbides, carbonitrides and nitrides (MXenes) are emerging members of two-dimensional materials that exhibit excellent redox activity, good hydrophilicity, electrical conductivity and flexibility. In addition, the chemical compositions of MXenes materials are easy to adjust and their layered structures are conducive to the adsorption of a large number of electrolyte ions. Therefore, anchoring electrochemically active materials on the MXenes frameworks is an effective way to prepare electrode materials with excellent sodium storage properties [122, 123]. When metal chalcogenides form heterostructures with MXenes, MXenes can enhance the electrical conductivity of the materials. Their open 2D structures can not only provide more channels for ion migration, but also expose more active sites for fast redox reactions [124, 125].

Wang et al. [95] prepared N-MXene-$MoS_2$ heterostructure. In this structure, $MoS_2$ was homogeneously anchored on MXene surfaces. N-MXene exhibited high electrical conductivity and open spaces. In addition, the robust heterointerfaces provided fast and unhindered electron migration channels. Therefore, the N-MXene-$MoS_2$ heterostructure exhibited outstanding rate properties and cycling performance (252.0 mAh $g^{-1}$ after 1000 cycles at 1.0 A $g^{-1}$).

Cao et al. [98] also used highly conductive $Ti_3C_2T_x$ MXene as the conductive layer, and prepared $Fe_{x-1}Se_x$ ($x$=2 or 3) heterostructure on carbon nanobelts, named $Fe_{x-1}Se_x$/MXene/FCRs. As a conductive layer, MXene provided sufficient sites for the self-assembly and growth of $Fe_{x-1}Se_x$ and prevented $Fe_{x-1}Se_x$ nanosheets from re-stacking and aggregation. Therefore, the electrode delivered excellent rate performance (**Figure 10**a) and cycling stability with a reversible $Na^+$ storage capacity of 348.1 mAh $g^{-1}$ after 2000 cycles at 10 A $g^{-1}$.

The preparation of chalcogenides/MXene heterostructures often requires cumbersome fabrication processes. In addition, the preparation process often uses dangerous HF, thus reducing the safety of the experiments and may cause accidental oxidation and degradation of MXenes [126]. The above two problems greatly hinder their further commercial application. Huang et al. [96] prepared a series of $Ti_3C_2T_x$ MXene/transition metal sulfides ($MS_y$, M =Fe, Co and Ni) heterostructures ($Ti_3C_2T_x$/$MS_y$).

Taking the $Ti_3C_2T_x/FeS_2$ heterostructure as an example and the preparation method was shown in Figure 10b. First, $Ti_3AlC_2$ MAX was immersed in $FeCl_2$ $4H_2O$ at 750 °C for 24 h. In this process, zero-valent Al was almost oxided to $Al^{3+}$ by $Fe^{2+}$, while $Fe^{2+}$ was reduced to Fe metal. Finally, $Ti_3C_2T_x/Fe$ was sulfurized in a tube furnace under Ar flow at 350 °C using thiourea ($CH_4N_2S$) as the sulfur source. Fe metal clusters reacted with $H_2S$ gas to form $FeS_2$, thereby in-situ growing $FeS_2$ nanoparticles in $Ti_3C_2T_x$ substrates via Ti-O-Fe bonds. The $Ti_3C_2T_x/FeS_2$ heterostructure exhibited dual sodium storage mechanisms (Figure 10c):

Pseudocapacitive intercalation reaction:

$$Ti_3C_2T_x + yNa^+ + ye^- \rightarrow Ti_3C_2T_xNa_y$$

Multi-step conversion reactions:

$$FeS_2 + zNa^+ + ze^- \rightarrow Na_zFeS_2$$

$$Na_zFeS_2 + (4-z)Na^+ + (4-z)e^- \rightarrow 2Na_2S + Fe$$

$Ti_3C_2T_x$ MXene provided smooth diffusion channels for electrons/ions and released volume stress of the material. In addition, the strong electron coupling at the heterointerfaces further promoted $Na^+$ and electron migration dynamics. Therefore, the $Ti_3C_2T_x/FeS_2$ heterostructures exhibited excellent rate performance (456.6 mAh $g^{-1}$ at 10 A $g^{-1}$) (Figure 10d) and long-term cycling stability (474.9 mAh $g^{-1}$ after 600 cycles at 5 A $g^{-1}$).

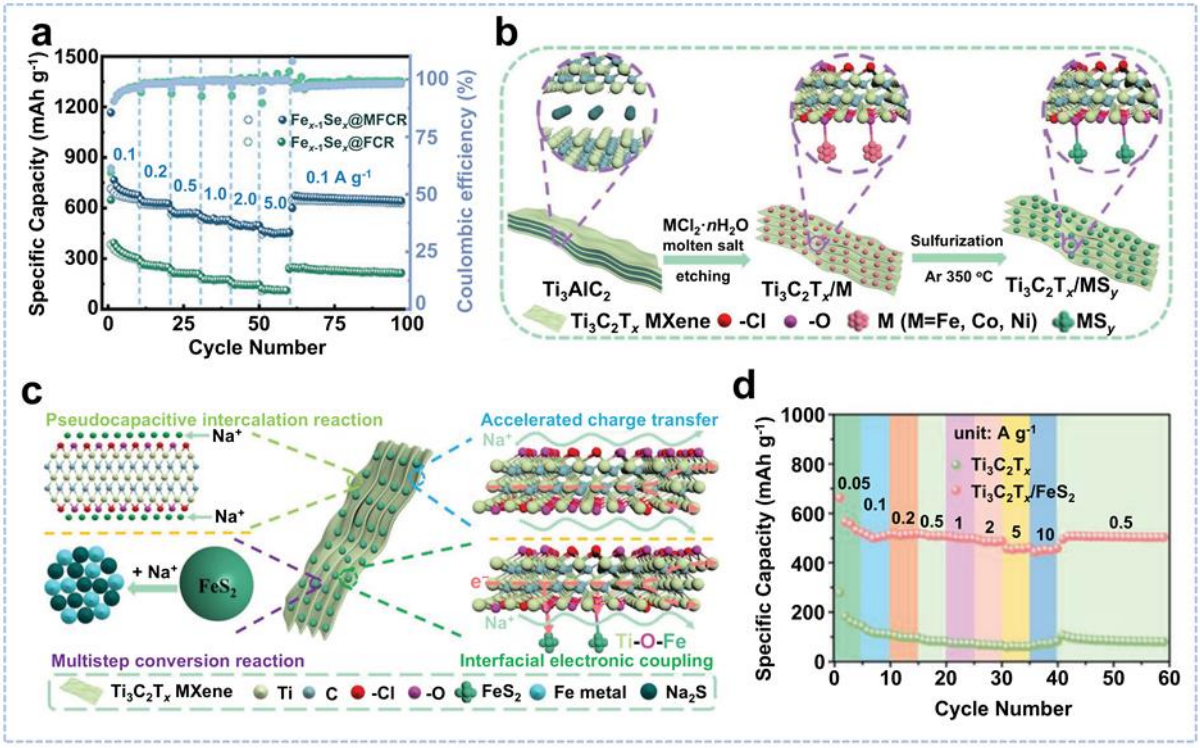

**Figure 10.** a) Rate capability of $Fe_{x-1}Se_x$/MXene/FCR. Reproduced with permission.[98] Copyright 2021, Wiley-VCH. b) Schematic diagram of the synthesis process of $Ti_3C_2T_x/MS_y$ heterostructure. c) Schematic diagram of the sodium storage mechanism and electrochemical performance enhancement mechanism of the $Ti_3C_2T_x/FeS_2$ heterostructure. d) Rate capability of $Ti_3C_2T_x/FeS_2$ heterostructure. Reproduced with permission.[96] Copyright 2021, Wiley-VCH.

## 5. Summary and outlook

This review provides detailed research status of the transition metal chalcogenide based heterostructures as electrode materials in recent years. Firstly, the definition of heterostructures is introduced. A heterojunction usually refers to the interface region formed by the contact of two semiconductor materials with different bandgap widths. According to the different semiconductor types, heterojunction can be divided into p-n junction, p-p or n-n junction and Schottky junction. Among the energy storage materials, p-n junction is the most widely used, which are interface regions composed of a p-type and an n-type semiconductor. Secondly, the promotion mechanisms of the sodium storage performance are reviewed. When two different materials are in contact, due to the difference in band gaps and work functions, carriers will diffuse between the two materials until the Fermi level reaches equilibrium. This process results in the induction of the BIEFs at the two-phase interfaces and causes charge redistribution. After forming the BIEFs, the electron accumulation regions will display the negative potentials, which are conducive to the ions adsorption and accelerate the ions/electrons migration, thereby enhancing the reaction kinetics of heterostructure materials. In addition, the construction of heterostructures also has advantages of enhancing the structural stability of the materials, generating more active sites and improving redox reactivity. Finally, based on the different building blocks, this review divides the metal chalcogenide based heterostructure materials into metal sulfides/sulfides heterostructures, metal sulfides/oxides heterostructures, metal sulfides/selenides heterostructures, metal selenides/selenides heterostructures, metal selenides/oxides heterostructures and MXene/chalcogenide heterostructures. Their research progress is further discussed by category.

Although some encouraging advancements have been reported in the application of these heterostructure anodes in SIBs, there are still many obstacles before the commercial

application of these materials and more researches and explorations are needed. Considering the future development of the heterostructure materials, the future prospects and potential directions of these materials are highlighted (**Figure 11**).

(1) More investigation in the mechanism research of the heterostructure is highly necessary. The heterointerfaces play a crucial role in improving sodium storage performance. In most studies, it is believed that the excellent electrochemical performance of heterostructures can be ascribed to the redistribution of the charges at the heterointerfaces, the generation of BIEFs and the synergistic effect of the heterostructure materials, which enhance the reaction kinetics, improve the structural stability, generate more active sites, etc. However, how charge redistribution and the formation of BIEFs affect the entire energy storage process, what kind of heterointerfaces have much better sodium storage performance are still unclear. Furthermore, the regulation of the BIEFs and their quantitative effect of strength BIEFs effect on the electrochemical properties are still unknown, which need numerous experimental and theoretical verification. Therefore, future research should pay more attention to these issues.

(2) Efficient computer algorithms technologies can be employed to the design and performance prediction of the heterostructures. With the development of the efficient computational materials science, DFT calculations, molecular dynamics (MD) simulations have been extensively used in the field of energy storage. In recent years, machine learning also has made exciting progress in materials screening and performance prediction. Therefore, more efficient computer algorithms are expected to be widely applied to guide the design, screening, performance prediction of the heterostructures, and further gain insights into the electrochemical mechanism from the perspective of the thermodynamics and kinetics, thereby reducing experimental research costs.

(3) Advanced *in-situ* characterization techniques are needed to reveal the positive effects of the heterointerfaces. There are still certain challenges in the precise characterization of the heterointerfaces and the evolution of the heterointerfaces during the electrochemical reactions. Different heterostructure materials show different interface changes in various discharged/charged states. It requires more advanced *in-situ* or real-time characterization techniques to monitor the formation of the heterostructures as well as structural changes of the heterointerfaces during the redox process. These can

provide more insightful information and further reveal the precise role of the heterostructures for energy storage mechanism explanation.

(4) Although metal chalcogenide based heterostructure materials have shown greatly improved electrochemical performance compared with pure metal chalcogenides, their practical applications are hindered by their mass preparation. On the other hand, most researches on heterostructure anode materials have focused on half-cells based on Na metal as the reference electrode. The electrochemical behaviors of these materials differ in half cells and full cells or pouch cells. It is necessary to apply heterostructures in full-battery systems to study their electrochemical properties, which need to match appropriate electrolytes and cathode materials, optimize various assembly parameters and the preparation process. Therefore, it is expected to develop simple mass preparation method to obtain high quality heterostructure materials and appropriate performance evaluation methods in pouch cells to further facilitate the practical application of the heterostructure anodes.

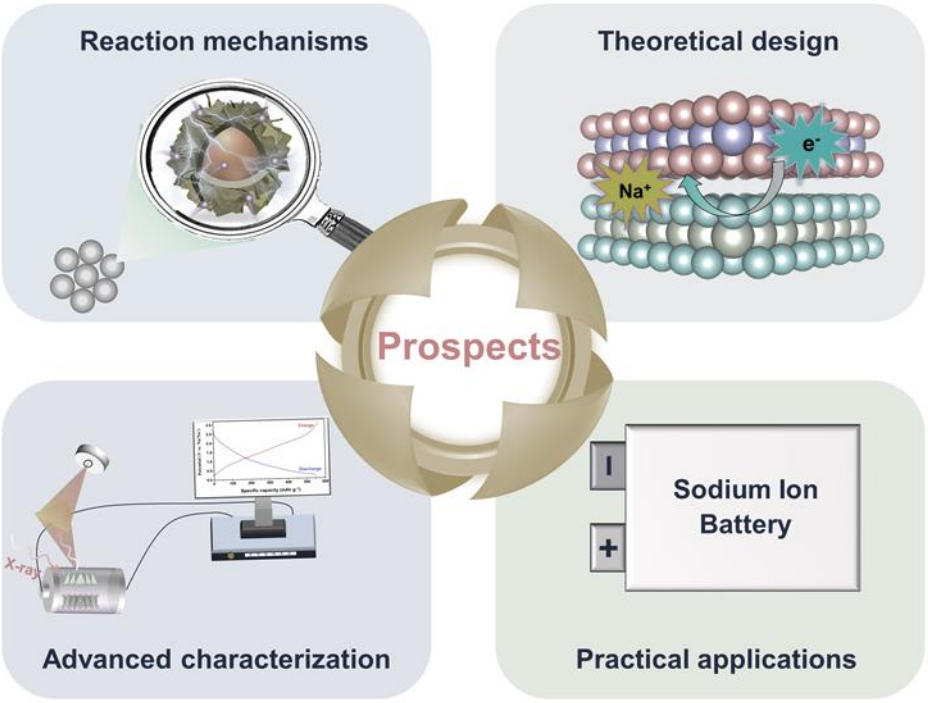


**Figure 11.** The future prospects and potential directions of these heterostructure materials.

**Acknowledgements**

This work was supported by the National Natural Science Foundation of China (No. 22109144), the Natural Science Foundation of Hubei province (2024AFB679), the Natural Science Foundation exploration program of Wuhan (2024040801020284)

and the Fundamental Research Funds for the Central Universities, China University of Geosciences (Wuhan) (No. 162301202673). Jiantao Li and Khalil Amine gratefully acknowledge support from the U.S. Department of Energy (DOE), Office of Energy Efficiency and Renewable Energy, Vehicle Technologies Office.

## References

[1] T. Yang, D. Luo, X. Zhang, S. Gao, R. Gao, Q. Ma, H. W. Park, T. Or, Y. Zhang, Z. Chen, *Nat. Sustain.* **2024**, *7*, 776–785.

[2] Y. Ye, R. Xu, W. Huang, H. Ai, W. Zhang, J. O. Affeld, A. Cui, F. Liu, X. Gao, Z. Chen, T. Li, X. Xiao, Z. Zhang, Y. Peng, R. A. Vila, Y. Wu, S. T. Oyakhire, H. Kuwajima, Y. Suzuki, R. Matsumoto, Y. Masuda, T. Yuuki, Y. Nakayama, Y. Cui, *Nat. Energy* **2024**, *9*, 643–653.

[3] K. Chen, P. Barai, O. Kahvecioglu, L. Wu, K. Z. Pupek, M. Ge, L. Ma, S. N. Ehrlich, H. Zhong, Y. Zhu, V. Srinivasan, J. Bai, F. Wang, *Nat. Commun.* **2024**, *15*, 430.

[4] H.-H. Ryu, H.-W. Lim, S. G. Lee, Y.-K. Sun, *Nat. Energy* **2023**, *9*, 47–56.

[5] R. Zhang, C. Wang, P. Zou, R. Lin, L. Ma, T. Li, I.-h. Hwang, W. Xu, C. Sun, S. Trask, H. L. Xin, *Nat. Energy* **2023**, *8*, 695–702.

[6] X. Zheng, R. Yu, J. Sun, Y. Chen, J. Chen, J. He, Y. Zhang, B. Han, G. Liao, J. Wu, R. Sun, C. Zhou, L. Mai, *Nano Energy* **2023**, *105*, 108000.

[7] X. Wang, Q. Zhang, C. Zhao, H. Li, B. Zhang, G. Zeng, Y. Tang, Z. Huang, I. Hwang, H. Zhang, S. Zhou, Y. Qiu, Y. Xiao, J. Cabana, C.-J. Sun, K. Amine, Y. Sun, Q. Wang, G.-L. Xu, L. Gu, Y. Qiao, S.-G. Sun, *Nat. Energy* **2024**, *9*, 184–196.

[8] Q. Wang, D. Zhou, C. Zhao, J. Wang, H. Guo, L. Wang, Z. Yao, D. Wong, G. Schuck, X. Bai, J. Lu, M. Wagemaker, *Nat. Sustain.* **2024**, *7*, 338–347.

[9] Y. Tang, Q. Zhang, W. Zuo, S. Zhou, G. Zeng, B. Zhang, H. Zhang, Z. Huang, L. Zheng, J. Xu, W. Yin, Y. Qiu, Y. Xiao, Q. Zhang, T. Zhao, H.-G. Liao, I. Hwang, C.-J. Sun, K. Amine, Q. Wang, Y. Sun, G.-L. Xu, L. Gu, Y. Qiao, S.-G. Sun, *Nat. Sustain.* **2024**, *7*, 348–359.

[10] Z. He, T. Han, W. Liu, C. Zhou, J. Sun, J. Zhou, Y. y. Li, *Adv. Energy Mater.* **2024**, *14*, 2303296.

[11] F. Zhang, B. He, Y. Xin, T. Zhu, Y. Zhang, S. Wang, W. Li, Y. Yang, H. Tian, *Chem. Rev.* **2024**, *124*, 4778–4821.

[12] Z. Hao, X. Shi, W. Zhu, Z. Yang, X. Zhou, C. Wang, L. Li, W. Hua, C. Q. Ma, S. Chou, *ACS Nano* **2024**, *18*, 9354–9364.

[13] Y. J. Guo, R. X. Jin, M. Fan, W. P. Wang, S. Xin, L. J. Wan, Y. G. Guo, *Chem. Soc. Rev.* **2024**, *53*, 7828–7874.

[14] J. Liu, J. Liu, M. Tang, J. Fu, X. Kuang, J. Ma, *Adv. Funct. Mater.* **2024**, *34*, 2314167.

[15] S. Qiao, Q. Zhou, M. Ma, H. K. Liu, S. X. Dou, S. Chong, *ACS Nano* **2023**, *17*, 11220–11252.

[16] Y. Chu, J. Zhang, Y. Zhang, Q. Li, Y. Jia, X. Dong, J. Xiao, Y. Tao, Q. H. Yang, *Adv. Mater.* **2023**, *35*, 2212186.

[17] H. Zheng, D. Ma, M. Pei, C. Lin, Y. Liu, S. Deng, R. Qiu, Y. Luo, W. Yan, J. Zhang, *Adv. Funct. Mater.* **2024**, DOI: 10.1002/adfm.202411651, 2411651.

[18] L. Fang, N. Bahlawane, W. Sun, H. Pan, B. B. Xu, M. Yan, Y. Jiang, *Small* **2021**, *17*, 2101137.

[19] J. H. Kim, G. D. Park, Y. C. Kang, *Chem. Eng. J.* **2021**, *410*, 128401.

[20] B. Chen, S. Sui, F. He, C. He, H. M. Cheng, S. Z. Qiao, W. Hu, N. Zhao, *Chem. Soc. Rev.* **2023**, *52*, 7802–7847.

[21] K. Nasrin, V. Sudharshan, K. Subramani, M. Sathish, *Adv. Funct. Mater.* **2022**, *32*, 2110267.

[22] J. Li, H. Yang, J. Wu, S. Sun, T. Zhai, H. Xia, *Small Struct.* **2022**, *3*, 2200022.

[23] S. H. Yang, S.-K. Park, G. D. Park, J. H. Kim, Y. C. Kang, *Chem. Eng. J.* **2021**, *417*, 127963.

[24] H. Fu, Q. Wen, P. Y. Li, Z. Y. Wang, Z. J. He, C. Yan, J. Mao, K. Dai, X. H. Zhang, J. C. Zheng, *Small Methods* **2022**, *6*, 2201025.

[25] Z. Zhao, G. Sun, Y. Zhang, R. Hua, X. Wang, N. Wu, J. Li, G. Liu, D. Guo, A. Cao, X. Liu, H. Hou, *Adv. Funct. Mater.* **2024**, *34*, 2314679.

[26] Y. Zhang, B. Han, Q. Gao, Z. Cai, C. Zhou, G. Hu, J. Li, R. Sun, *Nano Energy* **2024**, *128*, 109941.

[27] Y. Miao, Y. Xiao, S. Hu, S. Chen, *Nano Research* **2023**, *16*, 2347–2365.

[28] D. Sun, K. Liu, J. Hu, J. Zhou, *Small* **2021**, *17*, 2006374.

[29] E. Gabriel, C. Ma, K. Graff, A. Conrado, D. Hou, H. Xiong, *eScience* **2023**, *3*, 100139.

[30] G. D. Park, J. S. Park, J. K. Kim, Y. C. Kang, *Adv. Energy Mater.* **2021**, *11*, 2003058.

[31] P. Du, L. Cao, B. Zhang, C. Wang, Z. Xiao, J. Zhang, D. Wang, X. Ou, *Renew. Sust. Energy Rev.* **2021**, *151*, 111640.

[32] R. Ji, Z. Zhang, Y. J. Hofstetter, R. Buschbeck, C. Hänisch, F. Paulus, Y. Vaynzof, *Nat. Energy* **2022**, *7*, 1170–1179.

[33] J. Shin, S. Yang, Y. Jang, J. S. Eo, T. W. Kim, T. Lee, C. H. Lee, G. Wang, *Nat. Commun.* **2020**, *11*, 1412.

[34] A. Deng, Y. Sun, Z. Gao, S. Yang, Y. Liu, H. He, J. Zhang, S. Liu, H. Sun, S. Wang, *Nano Energy* **2023**, *108*, 108228.

[35] C. He, Q. Liu, H. Wang, C. Xia, F. M. Li, W. Guo, B. Y. Xia, *Small* **2023**, *19*, 2207474.

[36] J. Li, Y. Zhang, Y. Mao, Y. Zhao, D. Kan, K. Zhu, S. Chou, X. Zhang, C. Zhu, J. Ren, Y. Chen, *Angew. Chem. Int. Ed.* **2023**, *62*, e202303056.

[37] Z. Kong, L. Wang, S. Iqbal, B. Zhang, B. Wang, J. Dou, F. Wang, Y. Qian, M. Zhang, L. Xu, *Small* **2022**, *18*, 2107252.

[38] H. Shan, J. Qin, Y. Ding, H. M. K. Sari, X. Song, W. Liu, Y. Hao, J. Wang, C. Xie, J. Zhang, X. Li, *Adv. Mater.* **2021**, *33*, 2102471.

[39] S. Yang, C. Liu, H. Li, S. Wang, J. Choi, L. Li, *Energy Storage Mater.* **2021**, *39*, 278–286.

[40] S. Dong, C. Li, Z. Li, L. Zhang, L. Yin, *Small* **2018**, *14*, 1704517.

[41] C. Yang, X. Liang, X. Ou, Q. Zhang, H.-S. Zheng, F. Zheng, J.-H. Wang, K. Huang, M. Liu, *Adv. Funct. Mater.* **2019**, *29*, 1807971.

[42] Y. Zheng, T. Zhou, C. Zhang, J. Mao, H. Liu, Z. Guo, *Angew. Chem. Int. Ed.* **2016**, *55*, 3408–3413.

[43] C. Zhang, F. Han, F. Wang, Q. Liu, D. Zhou, F. Zhang, S. Xu, C. Fan, X. Li, J. Liu, *Energy Storage Mater.* **2020**, *24*, 208–219.

[44] J. Ni, M. Sun, L. Li, *Adv. Mater.* **2019**, *31*, 1902603.

[45] Y. Zhang, S. Wei, Z. Zhao, X. Pei, W. Zhao, J. Wang, X. Du, D. Li, *Small* **2022**, *18*, 2107258.

[46] G. Fang, Q. Wang, J. Zhou, Y. Lei, Z. Chen, Z. Wang, A. Pan, S. Liang, *ACS Nano* **2019**, *13*, 5635–5645.

[47] L. Fang, Z. Lan, W. Guan, P. Zhou, N. Bahlawane, W. Sun, Y. Lu, C. Liang, M. Yan, Y. Jiang, *Energy Storage Mater.* **2019**, *18*, 107–113.

[48] D. Wang, L. Cao, D. Luo, R. Gao, H. Li, D. Wang, G. Sun, Z. Zhao, N. Li, Y. Zhang, F. Du, M. Feng, Z. Chen, *Nano Energy* **2021**, *87*, 106185.

[49] E. Xu, Y. Zhang, H. Wang, Z. Zhu, J. Quan, Y. Chang, P. Li, D. Yu, Y. Jiang, *Chem. Eng. J.* **2020**, *385*, 123839.

[50] Z. Zhao, K. Li, C. Li, X. Pei, S. Zhang, Z. Liu, X. Du, D. Li, *ACS Appl. Mater. Interfaces* **2023**, *15*, 4011–4020.

[51] Y. Li, J. Qian, M. Zhang, S. Wang, Z. Wang, M. Li, Y. Bai, Q. An, H. Xu, F. Wu, L. Mai, C. Wu, *Adv. Mater.* **2020**, *32*, 2005802.

[52] S. Tang, Q. Yuan, J. Wang, T. Wang, W. Xiang, J. Li, J. S. Yu, *Energy Storage Mater.* **2024**, *68*, 103357.

[53] Y. Zhou, Q. Li, Q. Han, L. Zhao, Y. Liu, Y. Wang, Z. Li, C. Dong, X. Sun, J. Yang, X. Zhang, F. Jiang, *Small* **2023**, *19*, 2303742.

[54] Y. Su, B. Johannessen, S. Zhang, Z. Chen, Q. Gu, G. Li, H. Yan, J. Y. Li, H. Y. Hu, Y. F. Zhu, S. Xu, H. Liu, S. Dou, Y. Xiao, *Adv. Mater.* **2023**, *35*, 2305149.

[55] P. Song, J. Yang, C. Wang, T. Wang, H. Gao, G. Wang, J. Li, *Nanomicro. Lett.* **2023**, *15*, 118.

[56] Q. Li, R. Deng, Y. Chen, J. Gong, P. Wang, Q. Zheng, Y. Huo, F. Xie, X. Wei, C. Yang, D. Lin, *Small* **2023**, *19*, 2303642.

[57] D. Chen, Y. Wu, Z. Huang, K. Wang, X. Zhu, Z. Wang, J. Chen, *Chem. Eng. J.* **2023**, *457*, 141181.

[58] J. Zong, F. Wang, C. Nie, M. Zhao, S. Yang, *J. Mater. Chem. A* **2022**, *10*, 10651–10661.

[59] Y. Yan, P.-Q. Li, Z.-Y. Gu, W. Liu, J.-M. Cao, X.-L. Wu, *Chem. Eng. J.* **2022**, *432*, 134195.

[60] B. Yu, Y. Ji, X. Hu, Y. Liu, J. Yuan, S. Lei, G. Zhong, Z. Weng, H. Zhan, Z. Wen, *Chem. Eng. J.* **2022**, *430*, 132993.

[61] J. Wang, X. Yue, X. Cao, Z. Liu, A. M. Patil, J. Wang, X. Hao, A. Abudula, G. Guan, *Chem. Eng. J.* **2022**, *431*, 134091.

[62] L.-b. Tang, B. Zhang, T. Peng, Z.-j. He, C. Yan, J. Mao, K. Dai, X.-w. Wu, J.-c. Zheng, *Nano Energy* **2021**, *90*, 106568.

[63] J. Je, H. Lim, H. W. Jung, S. O. Kim, *Small* **2022**, *18*, 2105310.

[64] R. Fan, C. Zhao, J. Ma, J. Wu, T. He, Y. Dong, J. Dai, Y. Cai, *Small* **2022**, *18*, 2205175.

[65] R. Fan, C. Zhao, J. Ma, S. Lei, G. Liang, T. He, G. Zhu, Y. Cai, *J. Mater. Chem. A* **2022**, *10*, 939–949.

[66] J. Cheng, Z. Niu, Z. Zhao, X. Pei, S. Zhang, H. Wang, D. Li, Z. Guo, *Adv. Energy Mater.* **2022**, *13*, 2203248.

[67] S. Zhang, G. Wang, B. Wang, J. Wang, J. Bai, H. Wang, *Adv. Funct. Mater.* **2020**, *30*, 2001592.

[68] N. Shi, B. Xi, M. Huang, X. Ma, H. Li, J. Feng, S. Xiong, *Small* **2020**, *16*, 2000952.

[69] Y. Huang, X. Hu, J. Li, J. Zhang, D. Cai, B. Sa, H. Zhan, Z. Wen, *Energy Storage Mater.* **2020**, *29*, 121–130.

[70] L. Cao, X. Liang, X. Ou, X. Yang, Y. Li, C. Yang, Z. Lin, M. Liu, *Adv. Funct. Mater.* **2020**, *30*, 1910732.

[71] L. Cao, X. Gao, B. Zhang, X. Ou, J. Zhang, W. B. Luo, *ACS Nano* **2020**, *14*, 3610–3620.

[72] L. Yu, X. Tao, D. Sun, L. Zhang, C. Wei, L. Han, Z. Sun, Q. Zhao, H. Jin, G. Zhu, *Adv. Funct. Mater.* **2024**, *34*, 2311471.

[73] Y. Zhang, Y. Chen, Y. Jiang, J. Wang, X. Zheng, B. Han, K. Xia, Q. Gao, Z. Cai, C. Zhou, R. Sun, *Adv. Funct. Mater.* **2023**, *33*, 2212785.

[74] S. Huang, Y. Cao, F. Yao, D. Zhang, J. Yang, S. Ye, D. Yao, Y. Liu, J. Li, D. Lei, X. Wang, H. Huang, M. Wu, *Small* **2023**, *19*, 2207919.

[75] D. Cheng, L. Ye, A. Wei, G. Xu, Z. Cao, P. Zhu, Y. Chen, *Chem. Eng. J.* **2023**, *457*, 141243.

[76] Y. Zhou, M. Zhang, Q. Han, Y. Liu, Y. Wang, X. Sun, X. Zhang, C. Dong, F. Jiang, *Chem. Eng. J.* **2022**, *428*, 131113.

[77] S. Zhang, G. Yin, H. Zhao, J. Mi, J. Sun, L. Dang, *J. Mater. Chem. C* **2021**, *9*, 2933–2943.

[78] D. Gui, Z. Wei, J. Chen, L. Yan, J. Li, P. Zhang, C. Zhao, *J. Mater. Chem. A* **2021**, *9*, 463–471.

[79] C. Ma, Z. Xu, J. Jiang, Z. Ma, T. Olsen, H. Xiong, S. Wang, X.-Z. Yuan, *J. Mater. Chem. A* **2020**, *8*, 11011–11018.

[80] J. Wang, J. Cui, Z. Li, D. Zhang, H. Sun, H. Wang, Q. Wang, H. J. Woo, S. Ramesh, B. Wang, *Chem. Eng. J.* **2023**, *464*, 142764.

[81] T. He, W. Zhao, J. Hu, C. Deng, D. Yan, S. Huang, *Adv. Funct. Mater.* **2023**, *34*, 2310256.

[82] S. A. He, Z. Cui, Q. Liu, G. He, D. J. L. Brett, W. Luo, R. Zou, M. Zhu, *Small* **2021**, *17*, 2104186.

[83] T. Wang, D. Legut, Y. Fan, J. Qin, X. Li, Q. Zhang, *Nano Lett.* **2020**, *20*, 6199–6205.

[84] H. Li, Y. He, Q. Wang, S. Gu, L. Wang, J. Yu, G. Zhou, L. Xu, *Adv. Energy Mater.* **2023**, *13*, 2302901.

[85] H. Zhu, Z. Li, F. Xu, Z. Qin, R. Sun, C. Wang, S. Lu, Y. Zhang, H. Fan, *J. Colloid Interface Sci.* **2022**, *611*, 718–725.

[86] X. Liu, Z. Niu, Y. Xu, Z. Zhao, C. Li, Y. Yi, H. Guan, S. Zhang, X. Pei, D. Li, *Chem. Eng. J.* **2022**, *430*, 133176.

[87] F. Huang, L. Wang, D. Qin, Z. Xu, M. Jin, Y. Chen, X. Zeng, Z. Dai, *ACS Appl. Mater. Interfaces* **2022**, *14*, 1222–1232.

[88] Y. Zhang, X. L. Huang, P. Tan, S. Bao, X. Zhang, M. Xu, *Compos. Part B-Eng.* **2021**, *224*, 109166.

[89] S. Xiao, X. Li, W. Zhang, Y. Xiang, T. Li, X. Niu, J. S. Chen, Q. Yan, *ACS Nano* **2021**, *15*, 13307–13318.

[90] P. Liu, J. Han, K. Zhu, Z. Dong, L. Jiao, *Adv. Energy Mater.* **2020**, *10*, 2000741.

[91] W. Yan, M. Cao, S. Fan, X. Liu, T. Liu, H. Li, J. Su, *Compos. Part B-Eng.* **2021**, *213*, 108732.

[92] X. Ma, J. Luo, R. Jiang, W. Xiao, X. Shi, J. Xu, J. Sun, L. Shao, Z. Sun, *ACS Appl. Mater. Interfaces* **2024**, *16*, 18833–18842.

[93] P. Li, X. Guo, R. Zang, S. Wang, Y. Zuo, Z. Man, P. Li, S. Liu, G. Wang, *Chem. Eng. J.* **2021**, *418*, 129501.

[94] F. Zeng, M. Yu, W. Cheng, W. He, Y. Pan, Y. Qu, C. Yuan, *Small* **2020**, *16*, 2001905.

[95] T. Wang, K. Yao, Y. Hua, E. G. Shankar, R. shanthappa, J. S. Yu, *Chem. Eng. J.* **2023**, *457*, 141363.

[96] P. Huang, H. Ying, S. Zhang, Z. Zhang, W. Q. Han, *Adv. Energy Mater.* **2022**, *12*, 2202052.

[97] J. Ding, C. Tang, G. Zhu, W. Sun, A. Du, F. He, M. Wu, H. Zhang, *ACS Appl. Energy Mater.* **2021**, *4*, 846–854.

[98] J. Cao, L. Wang, D. Li, Z. Yuan, H. Xu, J. Li, R. Chen, V. Shulga, G. Shen, W. Han, *Adv. Mater.* **2021**, *33*, 2101535.

[99] J. Cao, J. Li, D. Li, Z. Yuan, Y. Zhang, V. Shulga, Z. Sun, W. Han, *Nanomicro. Lett.* **2021**, *13*, 113.

[100] L. Yu, Z. Li, W. Cai, H. Xie, J. Wang, Y. Ling, F. Huang, H. Li, G. Zhu, H. Jin, S. Wang, *Small* **2024**, *20*, 2404059.

[101] Y. Lin, Z. Qiu, D. Li, S. Ullah, Y. Hai, H. Xin, W. Liao, B. Yang, H. Fan, J. Xu, C. Zhu, *Energy Storage Mater.* **2018**, *11*, 67–74.

[102] H. Zhang, S. Zhang, B. Guo, L. J. Yu, L. Ma, B. Hou, H. Liu, S. Zhang, J. Wang, J. Song, Y. Tang, X. Zhao, *Angew. Chem. Int. Ed.* **2024**, *63*, e202400285.

[103] Y. Zhang, J. Li, X. Li, L. Shan, W. Zhao, J. Wang, Q. Gao, Z. Cai, C. Zhou, B. Han, K. Amine, R. Sun, *Nano Lett.* **2024**, *24*, 3331–3338.

[104] Y. Zhang, J. Wang, L. Shan, B. Han, Q. Gao, Z. Cai, C. Zhou, X. Tian, R. Sun, L. Mai, *Adv. Energy Mater.* **2023**, *14*, 2303464.

[105] J. Lee, C. Choi, H. Lee, S. Ma, J. Tan, G. Jang, S. G. Shim, Y. S. Park, J. Yun, D. W. Kim, J. Moon, *Adv. Energy Mater.* **2021**, *12*, 2103138.

[106] D. Cheng, L. Yang, R. Hu, J. Liu, M. Zhu, *Energy Environ. Mater.* **2020**, *4*, 229–238.

[107] J. M. Cao, M. Y. Ma, H. H. Liu, J. L. Yang, Y. Liu, K. Y. Zhang, F. A. Butt, Z. Y. Gu, K. Li, X. L. Wu, *Small* **2024**, *20*, 2311024.

[108] X. Wang, J. Zhao, Y. Chen, X. Zhang, K. Zhu, Q. Wang, J. Yan, D. Cao, G. Wang, *Small* **2024**, *20*, 2307747.

[109] X. Wang, X. Zhang, Y. Chen, J. Dong, J. Zhao, *Small* **2024**, *20*, 2312130.

[110] C. Dong, L. Wu, Y. He, Y. Zhou, X. Sun, W. Du, X. Sun, L. Xu, F. Jiang, *Small* **2020**, *16*, 2004580.

[111] Z. H. Sun, D. Y. Qu, D. X. Han, Z. Y. Gu, J. Z. Guo, X. X. Zhao, Y. M. Ma, B. L. Zhao, Z. Q. Song, X. L. Wu, L. Niu, *Adv. Mater.* **2024**, *36*, 2308987.

[112] C. Xu, K. Chen, J. Yang, G. Ma, Y. Wang, Z. Zhou, Z. Wu, S. Che, Z. Li, Y. Tu, Z. Xiao, D. Jiang, W. Yang, Y. Li, *Chem. Eng. J.* **2024**, *498*, 155353.

[113] H. Yin, H.-Q. Qu, Z. Liu, R.-Z. Jiang, C. Li, M.-Q. Zhu, *Nano Energy* **2019**, *58*, 715–723.

[114] Y. Huang, Z. Wang, Y. Jiang, S. Li, Z. Li, H. Zhang, F. Wu, M. Xie, L. Li, R. Chen, *Nano Energy* **2018**, *53*, 524–535.

[115] B. Zhao, Q. Liu, G. Wei, J. Wang, X.-Y. Yu, X. Li, H. B. Wu, *Chem. Eng. J.* **2019**, *378*, 122206.

[116] S. H. Yang, S.-K. Park, Y. C. Kang, *Chem. Eng. J.* **2019**, *370*, 1008–1018.

[117] J. Zhang, Y. Liu, H. Liu, Y. Song, S. Sun, Q. Li, X. Xing, J. Chen, *Small* **2020**, *16*, 2000504.

[118] J. Liu, S. Xiao, X. Li, Z. Li, X. Li, W. Zhang, Y. Xiang, X. Niu, J. S. Chen, *Chem. Eng. J.* **2021**, *417*, 129279.

[119] P. A. Shinde, V. Mahamiya, M. Safarkhani, N. R. Chodankar, M. Ishii, R. Ma, A. A. Ghaferi, L. K. Shrestha, K. Ariga, *Adv. Funct. Mater.* **2024**, *34*, 2406333.

[120] Y. Liu, Y. Xu, Y. Han, Z. Zhang, J. Xu, Y. Du, J. Bao, X. Zhou, *J. Power Sources* **2019**, *436*, 226860.

[121] F. Zhang, C. Xia, J. Zhu, B. Ahmed, H. Liang, D. B. Velusamy, U. Schwingenschlögl, H. N. Alshareef, *Adv. Energy Mater.* **2016**, *6*, 1601188.

[122] Y. Wu, P. Nie, L. Wu, H. Dou, X. Zhang, *Chem. Eng. J.* **2018**, *334*, 932–938.

[123] X. Wu, Z. Wang, M. Yu, L. Xiu, J. Qiu, *Adv. Mater.* **2017**, *29*, 1607017.

[124] F. Liu, S. Jin, Q. Xia, A. Zhou, L.-Z. Fan, *J. Energy Chem.* **2021**, *62*, 220–242.

[125] Y. Zhang, R. Zhan, Q. Xu, H. Liu, M. Tao, Y. Luo, S. Bao, C. Li, M. Xu, *Chem. Eng. J.* **2019**, *357*, 220–225.

[126] S. Zhang, H. Ying, P. Huang, J. Wang, Z. Zhang, T. Yang, W. Q. Han, *ACS Nano* **2020**, *14*, 17665–17674.

**Yuxiang Zhang** received his Bachelor's degree in Faculty of Materials Science and Chemistry from China University of Geosciences (CUG), Wuhan in 2019. He is currently working toward the Ph.D. degree at CUG (Wuhan) and his current research focuses on the anode materials for sodium-ion batteries.

**Bo Han** is an Associate Professor of Faculty of Materials Science and Chemistry at China University of Geosciences (CUG), Wuhan. He received his Ph.D. degree from CUG (Wuhan) in 2010. His current research focuses on computational materials science.

**Shuangshuang Tan** received his Ph.D. degree in Material Science and Engineering from Wuhan University of Technology in 2021. He is currently a lecturer at college of Materials Science and Engineering, Chongqing University. His current research focuses on the energy storage materials and devices, magnesium battery electrode materials and electrolytes.

**Qiang Gao** is an Associate Professor of Faculty of Materials Science and Chemistry at China University of Geosciences (CUG), Wuhan. He received his Ph.D. degree from Institute of Coal Chemistry, Chinese Academy of Sciences in 2009. His current research focuses on ion recognition detection and enrichment materials application, highly efficient environmental catalytic materials and water treatment technology.

**Zhao Cai** is a Distinguished Professor of Faculty of Materials Science and Chemistry at China University of Geosciences (CUG), Wuhan. He received his Ph.D. degree from Beijing University of Chemical Technology in 2018 and carried out postdoctoral research at Wuhan National Laboratory for Optoelectronics of Huazhong University of Science and Technology (2018-2022). His current research focuses on electrocatalysis and aqueous zinc-ion batteries.

**Chenggang Zhou** is a Professor of Faculty of Materials Science and Chemistry at China University of Geosciences (CUG), Wuhan. He received his Ph.D. degree from CUG (Wuhan) in 2008 and carried out postdoctoral research at National University of Singapore (2010-2011). His current research focuses on electrochemical energy storage, environment catalysis and computational materials science.

**Ruimin Sun** is a Distinguished Professor of Faculty of Materials Science and Chemistry at China University of Geosciences (CUG), Wuhan. She received her Ph.D. degree from Wuhan University of Technology (WUT) in 2018 and carried out postdoctoral research in Prof. Chunsheng Wang's group at University of Maryland, College Park (2018–2020). Her current research focuses on the energy storage materials and devices.

**Dr. Jiantao Li** is a research scientist in the Chemical Sciences and Engineering Division at Argonne National Laboratory. He earned his Ph.D. in Materials Science and Engineering from Wuhan University of Technology in 2019. Following his doctoral studies, he pursued postdoctoral research at Argonne under the mentorship of Dr. Khalil Amine. Dr. Li's research centers on electrochemical energy storage and conversion technologies, with a particular emphasis on the development and application of advanced synchrotron-based characterization techniques.

**Dr. Khalil Amine** is an Argonne Distinguished Fellow and leads the Advanced Battery Technology team at Argonne National Laboratory, focusing on the research and development of advanced materials and battery systems for HEV, PHEV, EV, and satellite applications. He also serves as an adjunct professor at Stanford University and the University of Chicago. In 2019, Dr. Amine was awarded the prestigious Global Energy Prize. He is a six-time recipient of the R&D 100 Award, often referred to as the "Oscar of technology and innovation." Additionally, he is a Fellow of the Electrochemical Society and serves as an associate editor for the journal *Nano Energy*. In recognition of his significant contributions to battery research, Dr. Amine has been elected as a Fellow of both the European Academy of Sciences and the National Academy of Inventors. These honors reflect his innovative work and prolific spirit in the field of battery technology.

This article reviews the development status of metal chalcogenide based heterostructures in SIBs, focusing on the definition, classification and role of heterostructures as well as the latest research progress of metal chalcogenide based heterostructure anodes in SIBs. Moreover, the future prospects and potential research directions of the heterostructures for batteries are discussed.

Yuxiang Zhang, Bo Han, Shuangshuang Tan, Qiang Gao, Zhao Cai, Chenggang Zhou, Jiantao Li*, Ruimin Sun*, Khalil Amine*

Interfacial engineering of metal chalcogenide-based heterostructures for advanced sodium-ion batteries

ToC figure